PHYSICAL REVIEW A VOLUME 46, NUMBER 9 1 NOVEMBER 1992

Excitation and ionization processes in slow collisions of ground-state and excited hydrogen atoms with protons

R. K. Janev
International Atomic Energy Agency, P.O. Box 200, A-1400 Vienna, Austria

P. S. Krstic
Institute of Physics, P.O. Box 57, YU-11001 Belgrade, Yugoslavia

(Received 27 September 1991; revised manuscript received 22 June 1992)

The collision dynamics in the $H^+ + H$ system is considered at low relative velocities within the concept of hidden adiabatic energy crossings in the complex plane of internuclear distance. Detailed information is provided on the topology of all series of hidden crossings in this system which are involved in the transitions between the states with principal quantum numbers $n \leq 4$ and in the promotion of these states into the continuum. This information is used to perform cross-section calculations for the $1s \rightarrow nl$ ($n = 2$–4), $n = 2 \rightarrow n = 3,4$, and $n = 3 \rightarrow n = 4$ excitation transitions and for ionization from the $n = 1$, 2, and 3 levels in the adiabatic energy region.

PACS number(s): 34.50.Fa, 34.50.Pi

I. INTRODUCTION

The usual expansion method based on quasimolecular states for description of slow heavy-particle collisions [1,2], even in its semiclassical version, contains conceptual difficulties associated with the Galilean invariance of the coupled equations for the rearrangement channels, or else, with the compatibility of adiabatic approximation with the physical boundary conditions [3,4]. Removal of these difficulties through formulation of the scattering problem in the Jacobi coordinates and introduction of an appropriate scale transformation of the internuclear distance [5] leads to transformation of the adiabatic basis into a dynamical one, for which the solution of both the eigenvalue problem and the corresponding coupled equations imposes formidable numerical (computer-time) requirements. For instance, due to the appearance of velocity-dependent terms in the instantaneous Hamiltonian, the variables in the simplest one-electron two-Coulomb-center eigenvalue problem are no longer separable.

Another approach to the dynamics of heavy-particle collisions at very low collision energies is to resort to the exact asymptotic solution of the dynamical coupled equations [4], which requires solution of the velocity-independent eigenvalue problem in the complex plane of internuclear distance R. The transitions between adiabatic states of the system are then entirely defined by the singularities of the analytically continued eigenenergies in the complex R plane [6–8], and the corresponding transition probabilities are given in terms of the well-known Landau contour integral [9]. This approach relies on the R analyticity of the electron-nucleus Coulomb interaction and the R analyticity of the entire electronic Hamiltonian $H(R)$ of the system in the adiabatic approximation. It appears that the singularities of the adiabatic eigenenergies in the complex R plane are square-root branch points connecting eigenstates with the same symmetry [6,7]. This is a consequence of the fact that off the real R axis, the Hamiltonian is no longer Hermitian and in a two-state degenerate subspace it assumes a Jordan rather than a diagonal form [4]. The branch point connecting two eigenenergy surfaces in the complex R plane ("hidden" crossing [6]) is seen as an "avoided crossing" of the corresponding potential-energy curves on the real R axis.

A prominent feature of the asymptotic method with Landau contour integration is that the calculation of a two-state transition probability requires only the knowledge of the eigenenergies in the complex R plane of corresponding adiabatic states. This is to be contrasted with the ordinary eigenstate expansion method using a real R basis where, apart from solving the set of coupled equations, knowledge of both the state energies (potential-energy curves) and the nondiagonal coupling matrix elements is required.

The asymptotic adiabatic method has so far been applied [7,10,11] to collision processes in the one-electron two-Coulomb-center system (Z_1,e,Z_2) ($Z_{1,2}$ being the nuclear charges), for which the necessary numerical codes for exact solution of the eigenvalue problem in the complex R plane, identification of energy singularities, and calculation of corresponding Landau contour integrals have been developed [6]. The processes considered in the previous applications of the method include the following: ionization in the $H^+ + H(1s)$ [7,11], $He^{2+} + H(1s)$ [10], and $H^+ + He^+(1s)$ [10] systems; the electron capture reaction $He^{2+} + H(1s) \rightarrow He^+$ [10]; and the $H^+ + He^+(1s) \rightarrow H^+ + He^+$ ($n = 2$) [10] excitation. Despite the fact that only a limited number of "hidden" crossings (or series of such crossings in the case of ionization) were included in these calculations, they have demonstrated the potential of the asymptotic adiabatic method for describing the collision dynamics in the adiabatic energy region and its competitiveness with the large-size coupled-channel calculations in predicting the inelastic cross sections.

In the present study we undertake a detailed investigation of the collision dynamics in the $H^+ + H$ (n) system

©1992 The American Physical Society

by using the asymptotic adiabatic method and including all the adiabatic states which correlate with the separated-atom states having principal quantum numbers $n \leq 4$, as well as a large number of additional higher adiabatic states involved in the promotion of $n \leq 4$ states to the continuum. The analysis of the topology of adiabatic energy surfaces in the complex R plane reveals the existence of additional series of branching points in the (Z_1,e,Z_2) system [12], which introduce a significant complexity in the collision dynamics and which have not been considered in the previous applications of the method [7,10,11]. A detailed account on the topology and singularities of the adiabatic energy surfaces of the $H^+ + H$ system in the complex R plane will be given in Sec. II. In Sec. III we briefly describe some basic features of the applied asymptotic approach to the collision dynamics of the $H^+ + H$ system. In Secs. IV and V we provide details of the cross-section calculations and results for the $H^+ + H(1s) \rightarrow H^+ + H(n=2,3,4)$, $H^+ + H^*$ $(n=2,3) \rightarrow H^+ + H^*$ $(n=4)$, and $H^+ + H^{(*)}$ $(n=1,2,3)$ $\rightarrow H^+ + H^+ + e$ processes in the energy region from ~ 0.5 to 15–20 keV/amu. The obtained results are compared with the available data from other theoretical and experimental investigations of these processes. In Sec. VI we give some concluding remarks regarding the applied method and obtained results.

We note that apart from providing a further insight in the collision dynamics of the $H^+ + H$ system in the adiabatic energy region and on the applicability of the asymptotic adiabatic method, the results of the present study are of interest in a number of plasma-fusion research areas in which low-energy cross-section data for collision processes involving excited hydrogen atoms and protons are required [13]. Guided partly by the same motivations, we have undertaken a similar systematic study of excitation, ionization, and electron capture processes in the $He^{2+} + H$ $(n \leq 4)$ system, the results of which will be reported elsewhere [14].

Atomic units $(e = m_e = \hbar = 1)$ will be used throughout this work, unless otherwise explicitly indicated.

II. TOPOLOGY OF POTENTIAL ENERGY SURFACES OF THE $H^+ + H$ SYSTEM IN THE COMPLEX R PLANE

A. Basic features of the eigenvalue problem for the (Z_1,e,Z_2) system in the complex R plane

The stationary Schrödinger equation of the two-center Coulomb problem (Z_1,e,Z_2),

$$\left[-\frac{1}{2}\Delta - \frac{Z_1}{|\mathbf{r}-\mathbf{R}/2|} - \frac{Z_2}{|\mathbf{r}+\mathbf{R}/2|}\right]\Phi(\mathbf{r},R) = E(R)\Phi(\mathbf{r},R) , \quad (1)$$

where R is the internuclear distance and $\mathbf{r}$ and $\mathbf{r}_{1,2} = \mathbf{r} \pm \mathbf{R}/2$ are the electron position vectors with respect to the midpoint of the internuclear distance and the centers 1,2, respectively, allow separation of variables in the prolate spheroidal coordinates,

$$\xi = \frac{r_1+r_2}{R}, \quad \eta = \frac{r_1-r_2}{R}, \quad \phi = \arctan(x/y) ,$$
$$1 \leq \xi < \infty, \quad -1 \leq \eta \leq 1, \quad 0 \leq \phi < 2\pi . \quad (2)$$

Representing $\Phi(\mathbf{r},R)$ in the form

$$\Phi(\mathbf{r},R) = [(\xi^2-1)(1-\eta^2)]^{-1/2} U(\xi) V(\eta) \exp(im\phi) , \quad (3)$$

one obtains from Eq. (1) the following equations for $U(\xi)$ and $V(\eta)$:

$$\left[\frac{d^2}{d\xi^2} - p^2 + \frac{a\xi - \lambda}{\xi^2-1} + \frac{1-m^2}{(\xi^2-1)^2}\right] U(\xi) = 0 , \quad (4a)$$

$$\left[\frac{d^2}{d\eta^2} - p^2 + \frac{b\eta + \lambda}{1-\eta^2} + \frac{1-m^2}{(1-\eta^2)^2}\right] V(\eta) = 0 , \quad (4b)$$

where

$$p = (-2E)^{1/2} R/2, \quad a = (Z_1+Z_2)R, \quad b = (Z_1-Z_2)R , \quad (5)$$

and λ is the separation constant. For real values of R, Eqs. 4(a) and 4(b) together with the boundary conditions

$$|U(1)| < \infty, \quad \lim_{\xi \to \infty} U(\xi) = 0 , \quad (6a)$$

$$|V(\pm 1)| < \infty \quad (6b)$$

define two boundary-value problems, with the eigenvalues $\lambda^{(\xi)}_{n_\xi m}(p,a)$ and $\lambda^{(\eta)}_{n_\eta m}(p,b)$, respectively. From the general theory of Sturm-Liouville problems, it follows that the quantum numbers n_ξ, n_η, and m are conserved when the parameter R varies.

From the obvious requirement $\lambda^{(\xi)}_{n_\xi m}(p,a) = \lambda^{(\eta)}_{n_\eta m}(p,b)$, one obtains the eigenvalue spectrum

$$E_\alpha(R) = E_{n_\xi n_\eta m}(R, Z_1, Z_2) . \quad (7)$$

In the classification of molecular states, the united-atom spherical quantum numbers (Nlm) are commonly used, and these are related to n_ξ, n_η, and m by

$$N = n_\xi + n_\eta + m + 1, \quad l = n_\eta + m . \quad (8)$$

The parabolic quantum numbers $[n \; n_1 \; n_2 \; m]$ $(n = n_1 + n_2 + m + 1)$, which are used to classify the electronic states in the separated-atom limit, can also be expressed in terms of (n_ξ, n_η, m), which together with (8) gives the correlation of the states in the two limits [2].

Several numerical codes presently exist for solving the eigenvalue problem (4)–(7) for real values of R in the discrete spectrum (see, e.g., Ref. [15]). Solov'ev [6] has used an analogous code for solving the problem in the complex R plane (For $\mathrm{Re}R > 0$), which will also be used in the present study (with a slight extension in the region $\mathrm{Re}R < 0$). One of the specific features of the eigenvalue problem (4)–(7) in the complex R plane is the existence of branching points R_c on the surfaces $E_\alpha(R)$ which connect them with other surfaces $E_\beta(R)$ having an appropriate symmetry. In the vicinity of these points the eigenenergy behaves as [4]

$$E(R)=E(R_c)+\text{const}\times(R-R_c)^{1/2} \tag{9}$$

and the $(R-R_c)^{-1/2}$ singularity of its derivative is used in the code as a signature for determination of the branch points R_c. The connection of two eigenenergies $E_\alpha(R)$ and $E_\beta(R)$ through a square-root branching point R_c means that $E_\alpha(R)$ and $E_\beta(R)$ are branches of a single analytic function $E(R)$ defined in the entire complex R plane. This property, which follows directly from the non-Hermitian character of $H(R)$ in the complex R plane and its reduction to a Jordan form in the vicinity of R_c, extends also to the corresponding eigenvectors, Φ_α and Φ_β [4], i.e., for a given symmetry they also represent branches of a single eigenvector $\Phi(\mathbf{r},R)$. It can be shown [4], however, that the normalization constant of the eigenvector $\Phi(\mathbf{r},R)$ becomes singular when $R\to R_c$, which induces singularities at $R=R_c$ in all (except the normalization) matrix elements calculated with Φ_α and Φ_β. For instance, the behavior of $\langle\Phi_\beta|\partial/\partial R|\Phi_\alpha\rangle$ near the branch point R_c is [6] $\sim(R-R_c)^{-1}$. If $\text{Im}R_c$ is not too large, the singularities of matrix elements at $R=R_c$ are seen as bell-shaped curves on the real R axis, while the branch point manifests itself as an avoided potential curve crossing. It should be noted that from the analyticity of $H(R)$ it follows that the branch points R_c always appear as complex conjugate pairs.

The previous eigenenergy calculations [6,7] for the (Z_1,e,Z_2) system in the complex R plane have revealed that the square-root branching points appear in series characterized by certain common features. Two different kinds of series have been identified which connect the adiabatic energy surfaces of the same symmetry according to different "selection" rules. These series of branching points, named S and T series, have characteristic distributions and typically appear in different regions of R. The S series appear at smaller values of $|R|$ where the classification of molecular states in terms of united-atom quantum numbers (Nlm) is appropriate, and are designated by S_{Nlm}. The majority of the branch points of T series appears at large $|R|$ values and they are designated by $T^{Z_1}_{n_1n_2m}$ and $T^{Z_2}_{n_1n_2m}$ according to the parabolic states around the Coulomb center (Z_1 or Z_2) to which the molecular states correlate.

The branch points of S_{Nlm} series connect the states $|Nlm\rangle$ and $|N+k,lm\rangle$, $k=1,2,3,\ldots$. With increasing k, the imaginary part of the branching point $R_{Nlm;k}$ increases dramatically, and from the point of view of collisional dynamics (see Sec. III), the branching points with $k\geq 2$ are not important. The first terms $(k=1)$ of the $S_{Nlm;k}$ series form superseries, S_{lm}, connecting pairwise the states $|Nlm\rangle$ and $|N+1,lm\rangle$ consecutively for all $N\geq l+1$. All the branch points R_{Nlm} of this (infinite) superseries are distributed in a small region Ω_{lm} in the complex R plane and have a limit point $R_{lm}=\lim_{N\to\infty}R_{Nlm}$. The S_{lm} superseries of branch points have been identified [8,16] as the physical basis for the Fano-Lichten [17] diabatic superpromotion phenomenon and the associated ionization mechanism in the slow heavy-particle collisions. In what follows, we shall refer to the S_{lm} superseries simply as the S_{lm} series.

The branch points of the series $T^{Z_{1,2}}_{n_1n_2m}$ connect the states $|Nlm\rangle$ and $|N+k,l+k,m\rangle$, $k=1,2,3,\ldots$, having the same "quasiradial" parabolic quantum number n_1 (and the same parity in the $Z_1=Z_2$ case) for all k. The branch points $R^{Z_{1,2}}_{n_1n_2m;k}$ for different k values are uniformly distributed on a steep straight line with a mutual interval [6] $\text{Im}(\Delta R_T)\simeq i2\pi(n_1+n_2+m+1)/(Z_1+Z_2)$. The branch points of the T series are related with the nonadiabatic transitions between the corresponding states at large real R values. Because of the large increase of $\text{Im}R^{Z_{1,2}}_{n_1n_2m;k}$ with k, only the first branch points $(k=1)$ in these series induce transitions with a considerable probability. The first branch points of the $T^{Z_{1,2}}_{n_1n_2m}$ series having the same value of n_2 form superseries $T^{Z_{1,2}}_{n_1m}$, which connect the states $|Nlm\rangle$ and $|N+1,l+1,m\rangle$ pairwise and in succession. The values of $\text{Re}R^{Z_{1,2}}_{n_1n_2m}$ increase significantly with increasing n_2.

On the receding stage of the collision, the $T^{Z_i}_{n_1m}$ superseries can also promote the $|Nlm\rangle$ state to the continuum [7,11]. In the case of a symmetric system, $Z_1=Z_2$, the adiabatic states acquire an additional symmetry (the parity) which is also conserved when R varies. Only the states with the same (g or u) parity are connected by the branch points of the $T^{Z;g,u}_{n_1n_2m}$ series. The branch points $R^{g,u}_{n_1n_2m}$ alternate. The correspondence between the (Nlm) and $[n\ n_1\ n_2\ m]$ quantum numbers in this case is [2,15]

$$N=n+n_2,\quad l=2n_2+m \qquad (l \text{ and } m \text{ of same parity})\,, \tag{10a}$$

$$N=n+n_2+1,\quad l=2n_2+m+1 \qquad (l \text{ and } m \text{ of different parity})\,. \tag{10b}$$

Because of the (g,u) symmetry, the T superseries in a symmetric system connect the states $|Nlm\rangle$ and $|N+2,l+2,m\rangle$.

The existence of the S_{lm} series of branch points connecting in the complex R plane, pairwise and in succession, all the eigenenergies of the (Z_1,e,Z_2) system having a specified symmetry, indicates that the energies $E_{Nlm}(R)$ are only different branches of a single analytic function $E_{lm}(R)$ (Riemann surface) defined on the entire complex R plane. Similarly, the $T^{Z_{1,2}}_{n_1n_2m}$ series also define Riemann surfaces with an infinite number of branches. In the next section we shall show that each of these Riemann surfaces is a multiply (infinite times) connected surface (see also Ref. [12]), and that, except at the branching points, each of the $E_{Nlm}(R)$ sheets is a smooth surface over the entire complex R plane, including the region $\text{Re}R<0$.

B. $E_{lm}(R)$ Riemann surfaces and S_{lm} series

Each of the S_{lm} series of branching points starts from the state $|Nlm\rangle$ with $N=l+1$ and includes the sequence of pairwise connected eigenenergies of the states

$$|Nlm\rangle_{g,u} \rightarrow |N+1,lm\rangle_{g,u} \rightarrow |N+2,lm\rangle_{g,u} \rightarrow \cdots \rightarrow |\infty,lm\rangle_{g,u} \tag{11}$$

having a given g,u symmetry. For a given m value, the parity of S_{lm} series interchanges, the first few series being $S^{g}_{1s\sigma}$, $S^{u}_{2p\pi}$, $S^{g}_{3d\delta}$, etc. The g,u labels can, therefore, be omitted from the series designation.

The identification of the square-root branch points $R^{N+i+1,lm}_{N+i,lm} \equiv R_{i,lm}$ of the above series in the complex R plane for the $\mathrm{H}^{+}+\mathrm{H}$ system was done by using the algorithm of Solov'ev [6] [the signature being the $(R-R_{i,lm})^{-1/2}$ singular behavior of the $E_{N+i,lm}(R)$ and $E_{N+i+1,lm}(R)$ surfaces at $R_{i,lm}$]. The algorithm is designed for calculation of $E_{N+i,lm}(R)$ and search for $R_{i,lm}$ only for $\mathrm{Re}R>0$, but with minor modifications it can be also used to identify $R_{i,lm}$ for R with negative values of $\mathrm{Re}R$ (except for the vicinity of the real axis). As an additional check for identification of the branching point, $R_{i,lm}$ serves the calculation of the contour integral,

$$\Delta_0^{(i)} = \left| \mathrm{Im} \int_{\mathrm{Re}R_{i,lm}}^{R_{i,lm}} \Delta E_{i,i+1}(R)\, dR \right| = \left| \mathrm{Im} \int_C E_{lm}(R)\, dR \right| , \tag{12}$$

where the contour C starts from the real R axis where $E_{lm}=E_{i,lm}(R)$, encompasses in the complex R plane the branch point $R_{i,lm}$, and returns back to the real R axis where $E_{lm}=E_{i+1,lm}(R)$. The value of $\Delta_0^{(i)}$ remains the same if the integration is carried out along the same contour but in the opposite direction. The quantity $\Delta_0^{(i)}$ is related to the generalized Massey parameter at the zero parameter (see Sec. III).

It has been shown in Ref. [12] that for $(l-m-\frac{1}{2})\geq 2$, new S series of branching points appear in the complex plane with $\mathrm{Re}R>0$ connecting the same $|N+i,lm\rangle$ and $|N+i+1,lm\rangle$ states. For a given (l,m) pair, the number of these points in the upper complex plane with $\mathrm{Re}R>0$ is equal to $\mathrm{Ent}[(l-m+1)/2]$, where $\mathrm{Ent}(x)$ denotes the integer part of x. Moreover, additional S series related to the sequence (11) appear also for $\mathrm{Re}R<0$. We shall designate these series as $S^{(\kappa)}_{lm}$ with $\kappa=0,1,2$. Each of these $S^{(\kappa)}_{lm}$ series has a limit point $R^{(\kappa)}_{\infty lm}=R^{(\kappa)}_{lm}$. The $R^{(\kappa)}_{lm}$ points are distributed in the complex R plane in such a way that

$$\mathrm{Re}R^{(0)}_{lm} > \mathrm{Re}R^{(1)}_{lm} > \mathrm{Re}R^{(2)}_{lm} > \cdots . \tag{13}$$

In Fig. 1, the first few branch points $R^{(\kappa)}_{i,lm}$ and the limit points $R^{(\kappa)}_{lm}$ of the series $S^{(0)}_{g\sigma}$, $S^{(1)}_{g\sigma}$, $S^{(2)}_{g\sigma}$, $S^{(0)}_{g\pi}$, and $S^{(1)}_{g\pi}$ are shown to illustrate their distributions in the complex R plane.

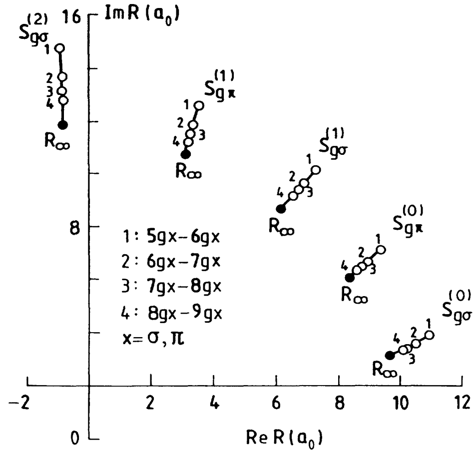

FIG. 1. Structure of the first three $S^{(\kappa)}_{g\sigma}$ and first two $S^{(\kappa)}_{g\pi}$ series in the complex R plane.

The branch-point distributions of other $S^{(\kappa)}_{lm}$ series have similar behavior. All branch points of a given $S^{(\kappa)}_{lm}$ series lie within a finite range $\{|R^{(\kappa)}_{Nlm}|-|R_{\infty lm}|^{(\kappa)}\}=\delta\rho^{(\kappa)}_{lm}$ of a few atomic units. $\delta\rho^{(\kappa)}_{lm}$ slightly increases with l, m, and κ.

The coordinates ($\mathrm{Re}R_c$; $\mathrm{Im}R_c$) of the first three branch points of the first several $S^{(\kappa)}_{lm}$ series with $m=0$, 1, and 2, and of the corresponding limit points $R^{(\kappa)}_{\infty lm}$, are given in Tables I and II. The values of the contour integrals (12), $\Delta_0^{(i)}$, associated with these branching points and their sum over the entire series, $\Delta^{(\kappa)}_{0,lm}=\sum_i \Delta_0^{(i)}$, are also given in the tables.

For a given m, the values $\Delta^{(\kappa)}_{0,lm}$ are roughly proportional to $l^{-1/2}$ and those for $\kappa=0$ and $m=0,1$ can approximately be represented as

$$\Delta^{(0)}_{0,l\sigma} \simeq 0.578 l^{-1/2}, \quad l \geq 1 , \tag{14a}$$

$$\Delta^{(0)}_{0,l\pi} \simeq 0.90 l^{-1/2}, \quad l \geq 2 . \tag{14b}$$

In the quasiclassical approximation, the limit points $R^{(\kappa)}_{lm}$ of the $S^{(\kappa)}_{lm}$ series can be calculated from the equation [8,12]

$$(m+1)/2 \pm i\gamma(R) = -\kappa, \quad \kappa=0,1,2,\ldots , \tag{15}$$

where

$$\gamma=\frac{1}{\pi}(2a)^{1/2}\left[\left[1+\frac{\lambda}{a}\right]K\left[\frac{a-\lambda}{2a}\right]-2E\left[\frac{a-\lambda}{2a}\right]\right], \quad a \geq \lambda , \tag{16a}$$

$$=\frac{2}{\pi}(a+\lambda)^{1/2}\left[K\left[\frac{\lambda-a}{\lambda+a}\right]-E\left[\frac{\lambda-a}{\lambda+a}\right]\right], \quad a \leq \lambda , \tag{16b}$$

$$\lambda=(l+\tfrac{1}{2})^2-b^2/8(l+\tfrac{1}{2})^{1/2}, \quad a=(Z_1+Z_2)R, \quad b=(Z_1-Z_2)R , \tag{17}$$

and $K(x)$ and $E(x)$ are the complete elliptic integrals. The solutions of Eq. (15) for $l=0-7$ and $m=0$ and $m=1$ in the upper-half R plane are shown in Table III. The notation $R_{\infty,lm}=|R_{\infty,lm}|\exp(+i\phi_{\infty,lm})$ is used, with $\phi_{\infty,lm}$ expressed in degrees. On the negative real axis ($\phi=180°$), Eq. (15) has an infinite number of solutions, only the first of which is shown in Table III. The number of $R^{(\kappa)}_{\infty,l\sigma}$ points lying in the upper half of the R plane is $\nu_\sigma=l$, while for the π states that number is $\nu_\pi=l$, for $l=1$ and 2, and $\nu_\pi=l-1$, for $l\geq 3$.

A series expansion of the elliptic integrals in Eq. (14) gives the following approximate solutions for $R^{(\kappa)}_{\infty,lm}$ (retaining only two terms in the expansion) [8,12]:

TABLE I. Coordinates ($\mathrm{Re}R_c$; $\mathrm{Im}R_c$) and Massey's parameters Δ_0 of the first few branch points of $S^{(\kappa)}_{Nl\sigma}$ superseries in the $H^+ + H$ system for $\mathrm{Re}R_c>0$.

$S^{(\kappa)}_{Nl\sigma}$		$N\leftrightarrow N+1$	$N+1\leftrightarrow N+2$	$N+2\leftrightarrow N+3$	$R^{(\kappa)}_{\infty,lm}\Big/\sum_i \Delta_0^{(i)}$
$S^{(0)}_{1s\sigma}$	R_c				−0.67;0.00
	Δ_0				
$S^{(0)}_{2p\sigma}$	R_c	0.7857;1.099	0.7676;1.050	0.7594;1.034	0.69;0.97
	Δ_0	0.3069	0.1042	0.0732	0.516
$S^{(0)}_{3d\sigma}$	R_c	2.961;1.965	2.869;1.850	2.828;1.805	2.69;1.72
	Δ_0	0.211	0.091	0.0479	0.427
$S^{(0)}_{4f\sigma}$	R_c	6.343;2.902	6.106;2.692	5.993;2.603	5.69;2.44
	Δ_0	0.1487	0.074	0.043	0.348
$S^{(1)}_{4f\sigma}$	R_c	2.603;7.508	2.461;7.047	2.303;6.839	2.18;6.37
	Δ_0	0.315	0.166	0.0975	0.809
$S^{(0)}_{5g\sigma}$	R_c	10.957;3.889	10.514;3.574	10.289;3.432	9.69;3.15
	Δ_0	0.11	0.060	0.037	0.291
$S^{(1)}_{5g\sigma}$	R_c	7.298;10.226	6.919;9.667	6.725;9.396	6.18;8.75
	Δ_0	0.246	0.142	0.09	0.754
$S^{(0)}_{6h\sigma}$	R_c	16.823;4.926	16.118;4.497	15.742;4.293	14.69;3.87
	Δ_0	0.0844	0.050	0.0324	0.248
$S^{(1)}_{6h\sigma}$	R_c	13.161;12.896	12.525;12.229	12.183;11.889	11.18;11.03
	Δ_0	0.196	0.121	0.0805	0.666
$S^{(2)}_{6h\sigma}$	R_c	5.473;19.82	5.038;18.608	4.815;17.98	4.16;16.32
	Δ_0	0.267	0.167	0.112	0.915
$S^{(0)}_{7i\sigma}$	R_c	23.96;6.00			20.69;4.58
	Δ_0	0.0669			0.216
$S^{(1)}_{7i\sigma}$	R_c	20.23;15.57			17.18;13.25
	Δ_0	0.160			0.593
$S^{(2)}_{7i\sigma}$	R_c	12.82;24.42			10.17;20.40
	Δ_0	0.222			0.857
$S^{(0)}_{8j\sigma}$	R_c	32.36;7.12			27.69;5.29
	Δ_0	0.0543			0.192
$S^{(1)}_{8j\sigma}$	R_c	28.54;18.28			24.19;15.45
	Δ_0	0.132			0.536
$S^{(2)}_{8j\sigma}$	R_c	21.28;28.90			17.17;24.31
	Δ_0	0.187			0.797
$S^{(3)}_{8j\sigma}$	R_c	9.51;38.16			6.63;30.80
	Δ_0	0.227			0.969

$$R^{(\kappa)}_{\infty,lm}=\frac{2}{Z_1+Z_2}\{(l+\tfrac{1}{2})^2-\tfrac{1}{2}(m+2\kappa+1)^2\pm i(m+2\kappa+1)[2(l+\tfrac{1}{2})^2-\tfrac{1}{4}(m+2\kappa+1)^2]^{1/2}\}\ . \tag{18}$$

Although approximate in character, this equation correctly predicts the number of $S^{(\kappa)}_{lm}$ series in the region ReR, and the fact that all $S^{(\kappa)}_{lm}$ series with $2\kappa \geq l-m$ have Re$R^{(\kappa)}_{\infty,lm}<0$. The distribution of $R^{(\kappa)}_{\infty,l\sigma}$ and $R^{(\kappa)}_{\infty,l\pi}$ points for $l=0$–7 is given in Fig. 2. This figure shows the "periodicity" of $R^{(\kappa)}_{\infty,lm}$ points and the alternation of $R^{(\kappa)}_{\infty,l\sigma}$ and $R^{(\kappa)}_{\infty,l\pi}$ with increasing κ. Some of these features follow also from the approximate equation (18). According to Eq. (18), the limit points $R^{(\kappa)}_{\infty,lm}$ satisfying the relation $m+2\kappa+1=$const have the same position in the complex R plane.

It should be noted that with a few exceptions occurring for large l and m (see Table II), the $S^{(\kappa)}_{lm}$ series of branching points with Re$R^{(\kappa)}_{\infty,lm}>0$ have the property

$$\{|R^{(\kappa)}_{Nlm}|-|R^{(\kappa)}_{\infty lm}|\}=\delta\rho^{(\kappa)}_{lm}>0\ ,$$

i.e., when R decreases from $R^{(\kappa)}_{Nlm}+\delta R$ towards $R^{(\kappa)}_{\infty,lm}$ they "promote" the $|Nlm\rangle$ state to the continuum on the

TABLE II. Coordinates (ReR_c; ImR_c) and Massey's parameters Δ_0 of the first few branch points of $S^{(\kappa)}_{Nl\pi}$ and $S^{(\kappa)}_{Nl\delta}$ superseries in the $H^+ + H$ system for Re$R_c>0$.

$S^{(\kappa)}_{Nl\pi}$		$N\leftrightarrow N+1$	$N+1\leftrightarrow N+2$	$N+2\leftrightarrow N+3$	$R^{(\kappa)}_{\infty,lm}\Big/\sum_i \Delta_0^{(i)}$
$S^{(0)}_{2p\pi}$	R_c				−0.638;1.29
	Δ_0				
$S^{(0)}_{3d\pi}$	R_c	1.291;3.395	1.292;3.197	1.286;3.118	1.27;3.10
	Δ_0	0.32	0.142	0.076	0.697
$S^{(0)}_{4f\pi}$	R_c	4.743;5.313	4.554;4.986	4.462;4.842	4.37;4.65
	Δ_0	0.241	0.124	0.073	0.607
$S^{(0)}_{5g\pi}$	R_c	9.384;7.147	8.976;6.711	8.767;6.504	8.37;7.59
	Δ_0	0.184	0.104	0.066	0.527
$S^{(1)}_{5g\pi}$	R_c	3.569;12.691	3.371;11.897	3.270;11.511	3.11;10.78
	Δ_0	0.288	0.167	0.106	0.870
$S^{(0)}_{6h\pi}$	R_c	15.248;8.99			13.37;7.59
	Δ_0	0.144			0.462
$S^{(1)}_{6h\pi}$	R_c	8.114;14.004			8.11;14.00
	Δ_0	0.234			0.803
$S^{(0)}_{7i\pi}$	R_c	22.34;10.84			19.38;9.04
	Δ_0	0.116			0.409
$S^{(1)}_{7i\pi}$	R_c	16.80;20.11			14.12;17.09
	Δ_0	0.193			0.735
$S^{(2)}_{7i\pi}$	R_c	6.982;27.99			5.33;22.99
	Δ_0	0.244			0.945
$S^{(0)}_{4f\delta}$	R_c	1.47;6.54			2.18;6.37
	Δ_0	0.29			0.796
$S^{(0)}_{5g\delta}$	R_c	6.20;9.86			6.18;8.75
	Δ_0	0.234			0.711
$S^{(0)}_{6h\delta}$	R_c	12.21;12.79			11.18;11.03
	Δ_0	0.189			0.635
$S^{(1)}_{6h\delta}$	R_c	4.14;18.81			4.16;16.32
	Δ_0	0.26			0.911

TABLE III. Coordinates ($|R_\infty|$; ϕ_∞^0) of the limit points $R_{\infty,lm}$ of the $S_{l\sigma}^{(\kappa)}$ and $S_{l\pi}^{(\kappa)}$ series for $\phi \leq \pi$.

lm	κ	0	1	2	3	4	5
$s\sigma$	$\|R_\infty\|$	0.67					
	ϕ_∞^0	180					
$p\sigma$	$\|R_\infty\|$	1.190	4.87				
	ϕ_∞^0	54.574	180				
$d\sigma$	$\|R_\infty\|$	3.193	3.792	13.53			
	ϕ_∞^0	32.595	102.643	180			
$f\sigma$	$\|R_\infty\|$	6.191	6.733	8.146	26.53		
	ϕ_∞^0	23.201	71.13	127.067	180		
$g\sigma$	$\|R_\infty\|$	10.189	12.374	11.931	14.337	43.85	
	ϕ_∞^0	18.008	54.767	94.134	143.738	180	
$h\sigma$	$\|R_\infty\|$	15.191	15.705	16.842	18.848	22.439	65.51
	ϕ_∞^0	14.750	44.604	75.700	110.012	158.099	180
$p\pi$	$\|R_\infty\|$	1.439	11.12				
	ϕ_∞^0	116.316	180				
$d\pi$	$\|R_\infty\|$	3.350	4.539	23.48			
	ϕ_∞^0	67.722	151.008	180			
$f\pi$	$\|R_\infty\|$	6.381	7.287	12.48			
	ϕ_∞^0	46.778	97.158	180			
$g\pi$	$\|R_\infty\|$	10.375	11.220	12.925	26.62		
	ϕ_∞^0	36.218	73.907	116.367	180		
$h\pi$	$\|R_\infty\|$	15.374	16.179	17.703	20.358	44.68	
	$\phi_{\infty 0}$	29.583	59.917	92.234	130.198	180	

approaching stage of the nuclei. On the usual adiabatic energy diagrams, $\mathrm{Re}E_{Nlm}(\mathrm{Re}R)$, only the promoting features of $S_{lm}^{(0)}$ series with $l \geq 3$ can be observed (as series of avoided potential curve crossings). This is shown in Fig. 3(a) for the $S_{f\sigma}^{(0)}$ series. The promoting character of the series of pseudocrossings is well recognizable only for the first few terms of the series. If we represent R in the form $R = |R| \exp(i\phi)$, the viewing plane $(\mathrm{Re}E,\phi)$ of the $S_{f\sigma}^{(0)}$ series in Fig. 3(a) is defined by the direction $\phi=0$. By rotating the viewing plane around the $R=0$ axis (i.e., by increasing ϕ), the promoting character of $S_{f\sigma}^{(0)}$ becomes more and more apparent and at $\phi=\phi_{\infty,f\sigma}^{(0)}-2°$, the $S_{f\sigma}^{(0)}$ series of hidden crossings is seen as shown in Fig. 3(b). If we continue to rotate the viewing plane beyond $\phi_{\infty,f\sigma}^{(0)}$ and approach the $S_{f\sigma}^{(1)}$ series, at the position $\phi=\phi_{\infty,f\sigma}^{(1)}-2°$ we see the pseudocrossing series originating from the $S_{f\sigma}^{(1)}$ series of hidden crossings, as shown in Fig. 3(c). The promoting character of the $S_{h\sigma}^{(0)}$ series is barely observable in the $(\mathrm{Re}E,\phi=0)$ potential curve diagram. However, from the position $\phi=\phi_{\infty,h\sigma}^{(0)}-2°$ of the viewing plane, the promoting character is clearly seen [Fig. 4(a)]. At still larger values of ϕ, the promoting pseudocrossing series due to the $S_{h\sigma}^{(1)}$ and $S_{h\sigma}^{(2)}$ series of hidden crossings also become observable [Figs. 4(b) and 4(c)].

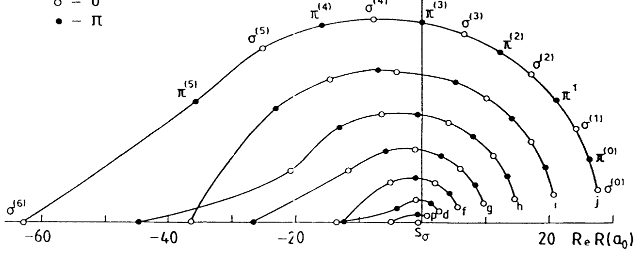

FIG. 2. Distribution of the limit points $R_{\infty,lm}^{(\kappa)}$ of the $S_{l\sigma}^{(\kappa)}$ and $S_{l\pi}^{(\kappa)}$ series for $l=0,1,2,\ldots,7$.

In the vicinity of a branch point, the adiabatic energy surface $\mathrm{Re}E_{Nlm}(R)$ is strongly deformed due to the infinite value of its derivative at the position of the branching point.

In Figs. 5(a) and 5(b), we show the three-dimensional (3D) plots of the $\mathrm{Re}E_{4f\sigma}$ and $\mathrm{Re}E_{6h\sigma}$ surfaces, respectively, on which the branching points $R_{4f\sigma,5f\sigma}^{(\kappa)}$ ($\kappa=0,1$) and $R_{6h\sigma,7h\sigma}^{(\kappa)}$ ($\kappa=0,1,2$), as well as the corresponding branch cuts, can clearly be seen. Figures 6(a) and 6(b) show the contour plots of these surfaces for Re$E > -0.25$, with a step $\Delta(\mathrm{Re}E)=0.002$, on which the branch cuts are also clearly seen.

With a slight extension of the numerical code [6] for calculation of the energy of (Z_1,e,Z_2) system in the complex R plane, it is possible also to calculate the energy $E_{Nlm}(R)$ in the region with Re$R<0$. Figures 7(a) and 7(b), show the surfaces Re$E_{5g\sigma}(R)$ and Im$E_{5g\sigma}(R)$ in the region Re$R \geq -5$ and Im$R \geq 0$, on which the first branch points (and corresponding branch cuts) of the series $S^{(\kappa)}_{g\sigma}$, $\kappa=0,1,2$, can be seen. It should be noted that both ReE and ImE are continuous at Re$R=0$. It can be also seen from the 3D plot on Fig. 7(a) that while the gradient $d(\mathrm{Re}E)/d(\mathrm{Re}R)$ of Re$E_{5g\sigma}$ in the vicinity of the branch points with $\phi^{(\kappa)}_{5g\sigma}<\pi/2$ (i.e., for $\kappa=0$ and $\kappa=1$) is negative, its value near the branch point $R^{(2)}_{5g\sigma}$ ($\phi>\pi/2$) is positive. This indicates that the series $S^{(2)}_{5g\sigma}$ has an "antipromoting" character.

The principal result of the above discussions is that the specific E_{Nlm} sheets of the Riemann surface $E_{lm}(R)$ with a given symmetry are multiply connected through the branch points of the series $S^{(\kappa)}_{lm}$, where κ takes an unlimited number of values.

All the $S^{(\kappa)}_{lm}$ series with $\phi<\pi/2$ have promoting character (i.e., $\mathrm{Re}R^{(\kappa)}_{Nlm} > \mathrm{Re}R^{(\kappa)}_{N+1,lm} > \mathrm{Re}R^{(\kappa)}_{\infty,lm}$), while those lying in the second quadrant of the upper half plane ($\pi>\phi>\pi/2$) have an antipromoting character ($\mathrm{Re}R^{(\kappa)}_{\infty lm} > \mathrm{Re}R^{(\kappa)}_{Nlm}$). Therefore, if the $S^{(\kappa)}_{lm}$ series in the region $\phi<\pi/2$ are associated with the promotion of the system into the continuum, the $S^{(\kappa)}_{lm}$ series in the region $\pi>\phi>\pi/2$ should be related to the nonadiabatic capture of a continuum electron in the $|Nlm\rangle$ state. These aspects of the hidden-crossing adiabatic theory have not been investigated as yet.

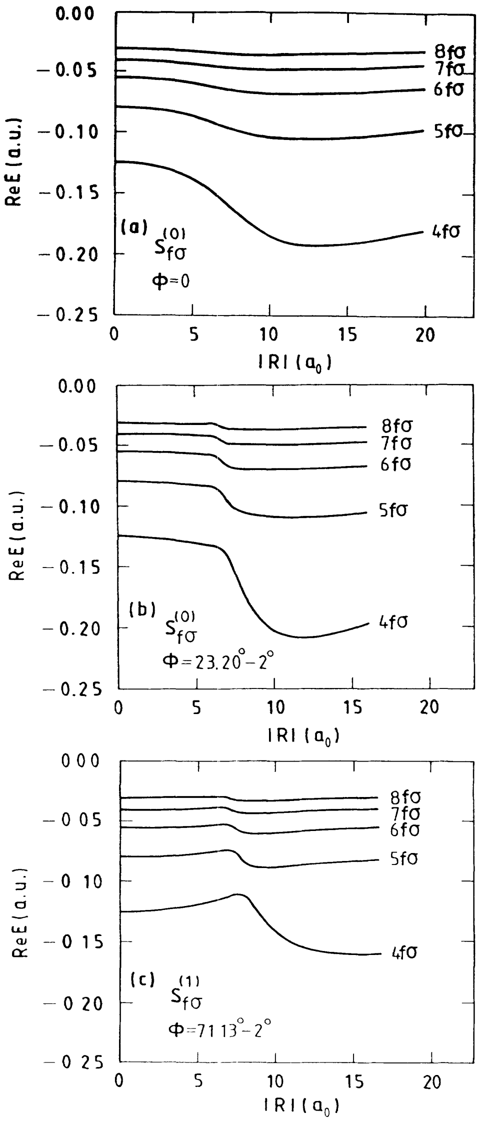

FIG. 3. Cross sections through the $4f\sigma$-$8f\sigma$ adiabatic energy-surfaces by the "viewing" planes (ReE,$\phi=0$) (a), (ReE,$\phi^{(0)}_{\infty}-2°$) (b), and (ReE,$\phi^{(1)}_{\infty}-2°$) (c).

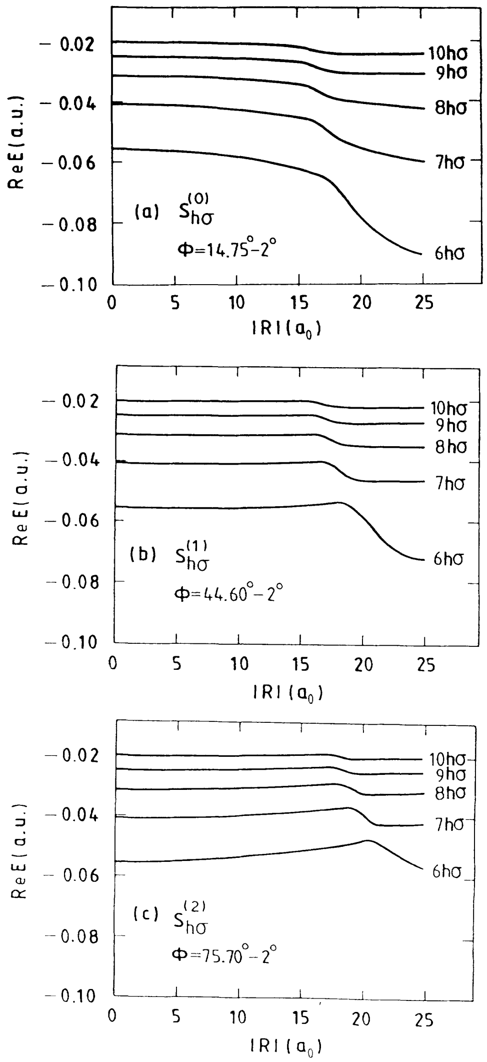

FIG. 4. View on the $S^{(\kappa)}_{h\sigma}$ series of hidden crossings from the vertical planes (ReE,$\phi^{(\kappa)}_{\infty}-2°$) for (a) $\kappa=0$, (b) $\kappa=1$, and (c) $\kappa=2$.

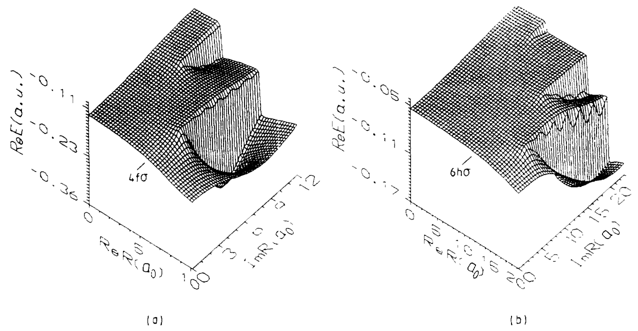

FIG. 5. Three-dimensional plots of adiabatic energy surfaces (a) $\mathrm{Re}E_{4f\sigma}(R)$ and (b) $\mathrm{Re}E_{6h\sigma}(R)$ for complex values of R.

C. $T_{n_1n_2m}$ series and $T^s_{n_1m}$ superseries

Because of the g,u symmetry of the (Z,e,Z) system, the $T^{(g,u)}_{n_1n_2m}$ series connect the states $|Nlm\rangle$ and $|N+k,l+k,m\rangle$ with $k=2,4,6,\ldots$. For instance, the series $T^{(g)}_{000}$ consists of branch points connecting the states $1s\sigma_g$-$3d\sigma_g$, $1s\sigma_g$-$5g\sigma_g$, $1s\sigma_g$-$7i\sigma_g$, $\ldots$, while the series $T^{(u)}_{000}$ contains the branch points connecting the states $2p\sigma_u$-$4f\sigma_u$, $2p\sigma_u$-$6h\sigma_u$, $2p\sigma_u$-$8j\sigma_u$, $\ldots$. (For the states with $l=7,8,\ldots$, we use the nonstandard notation $j,k,\ldots$.) The branch points of the series $T^{(g)}_{n_1lm}$ and $T^{(u)}_{n_1lm}$ lie on the same rather steep line in the complex R plane as shown for the T_{000} and T_{010} series of the $(\mathrm{H}^+,e,\mathrm{H}^+)$ system in Fig. 8 (the dashed lines). Because of the sharp increase of $\mathrm{Im}R^{n_1n_2+k,m}_{n_1n_2m}$ with increasing k [by $\pi(n_1+n_2+m+1)$, for the $Z_1=Z_2$ case], only the first branching of the $T^{(g,u)}_{n_1n_2m}$ series is important from the point of view of the collision dynamics (see Sec. III). For large values of R, approximate analytic expressions can be derived for the first branch points of the $T^{(g,u)}_{n_1n_2m}$ series [10]:

$$R^{(g)}_{n_1n_2m} \simeq 6n[n-n_\xi+(m+1)/2]+1+i4n \ , \tag{19a}$$

$$R^{(u)}_{n_1n_2m} \simeq 6n[n-n_\xi+(m+1)/2]+1+i8n \ , \tag{19b}$$

where

$$n_\xi=N-l-2m-1, \quad n=n_1+n_2+m+1 \ .$$

As mentioned in the preceding section, the first branch points of the series $T_{n_1n_2m}$ with the same n_1 and m and $n_2 \geq n-n_1-m-1$ form a superseries $T^s_{n_1m}$. From each $|Nlm\rangle$ state, with $l \leq N-1$, a $T^s_{n_1m}$ (or T^s_{Nlm}) superseries may start. The first few $T^s_{n_1m}$ superseries in the $\mathrm{H}^++\mathrm{H}$

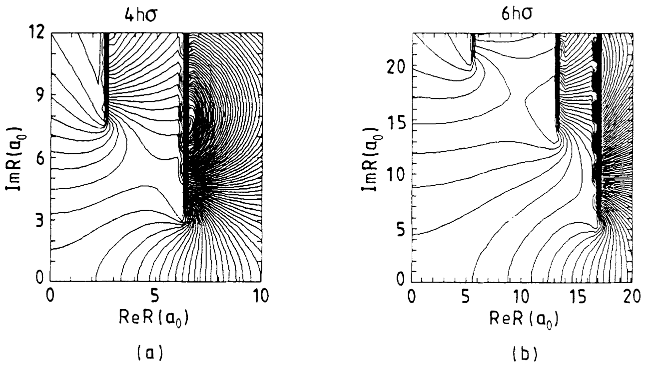

FIG. 6. Contour plots of the adiabatic energy surfaces (a) $\mathrm{Re}E_{4f\sigma}(R)$ and (b) $\mathrm{Re}E_{6h\sigma}(R)$ for $\mathrm{Re}E>-0.25$ in the complex R plane.

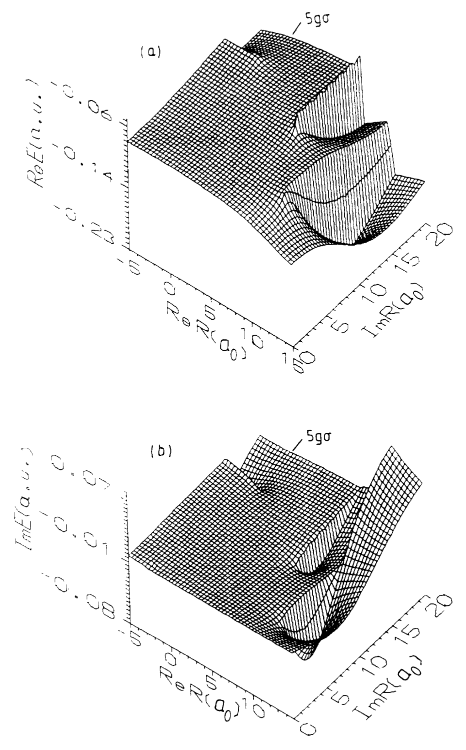

FIG. 7. (a) Real and (b) imaginary parts of the energy of $5g\sigma$ adiabatic state in the complex R plane for $\mathrm{Re}R \geq -5$ and $\mathrm{Im}R \geq 0$.

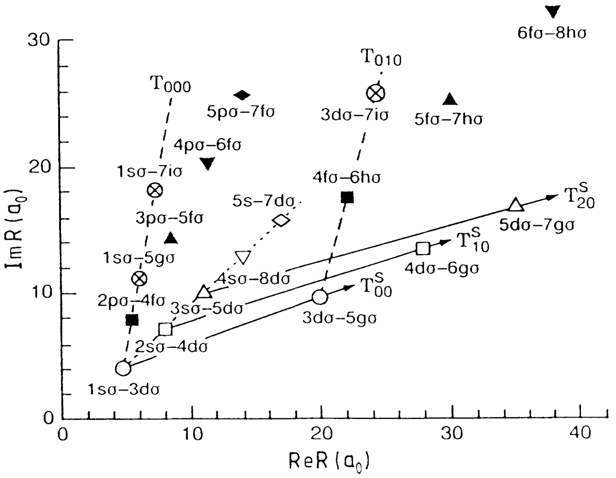

FIG. 8. Distribution in the complex R plane of the first several branching points of the superseries $T^s_{Ns\sigma}$ ($N=0$–5, open symbols) and $T^s_{Np\sigma}$ ($N=0$–5, solid symbols). Crossed circles are higher members of the T_{000} and T_{010} series.

TABLE IV. Coordinates (ReR_c; ImR_c) and Massey's parameters Δ_0 for the first few branch points of $T_{Nl\sigma}{}^{s}$ superseries in the H$^+$+H system, and the values of $\Delta_{0,\text{tot}}$.

$T^s_{Nl\sigma}$		$Nl \to N+2, l+2$	$N+2, l+2 \to N+4, l+4$	$N+4, l+4 \to N+6, l+6$	$\Delta_{0,\text{tot}}$
$T^s_{1s\sigma}$	R_c	4.784;4.143	20.115;9.45	45.499;15.307	
	Δ_0	1.271	0.43	0.216	2.06
$T^s_{2s\sigma}$	R_c	7.904;7.242	27.854;13.156	61.00;16.00	
	Δ_0	0.3555	0.1936	0.141	0.691
$T^s_{2p\sigma}$	R_c	5.44;7.80	22.18;17.54	49.22;28.39	
	Δ_0	3.5[a]	1.12	0.542	1.94
$T^s_{3s\sigma}$	R_c	10.958;9.924	35.326;16.503	76.00;20.00	
	Δ_0	0.1585	0.1074	0.096	0.359
$T^s_{3p\sigma}$	R_c	8.661;14.408	30.426;25.139	61.00;32.00	
	Δ_0	0.955	0.524	0.283	1.76
$T^s_{4p\sigma}$	R_c	11.551;20.023	38.207;31.188	106;20.0	
	Δ_0	0.446	0.298	0.096	0.840

[a] $4f\sigma$ is a quasistationary state for impact parameters $b \le 5a_0$. The value quoted for $\Delta_{0,\text{tot}}$ refers to the $T^s_{4f\sigma}$ superseries.

system connect the sequence of following states:

$$T^{s,g}_{00}\ (=T^s_{1s\sigma_g}):\ 1s\sigma_g\text{-}3d\sigma_g\text{-}5g\sigma_g\text{-}7i\sigma_g\text{-}\cdots\ ,$$

$$T^{s,u}_{00}\ (=T^s_{2p\sigma_u}):\ 2p\sigma_u\text{-}4f\sigma_u\text{-}6h\sigma_u\text{-}8j\sigma_u\text{-}\cdots\ ,$$

$$T^{s,g}_{10}\ (=T^s_{2s\sigma_g}):\ 2s\sigma_g\text{-}4d\sigma_g\text{-}6g\sigma_g\text{-}8i\sigma_g\text{-}\cdots\ .$$

The first several branching points of the $T^s_{Ns\sigma}$ and $T^s_{Np\sigma}$ superseries are shown in Fig. 8. It can be seen that the branch points of a superseries lie on a straight line, as do the branch points connecting the states with different N but the same l and m values (as shown by the dotted line in Fig. 8 for the $Ns\sigma$ states). The coordinates of the first few branching points for the first several $T^s_{Nl\sigma}$, $T^s_{Nl\pi}$, and $T^s_{Nl\delta}$ superseries of the H$^+$+H system are given in Tables IV and V, together with the values $\Delta_{0,i}$ of the corresponding contour integral (12), and their sum $\Delta_{0,\text{tot}}=\sum_i \Delta_{0,i}$.

In order to obtain an insight on the behavior of adiabatic energy surfaces Re$E_{Nlm}(R)$ in the vicinity of a T-type branching point, we show in Fig. 9(a) the 3D plot of the surface Re$E_{3d\sigma}(R)$. The strong deformation of the

TABLE V. Coordinates (ReR_c; ImR_c) and Massey's parameters Δ_0 for the first few branch points of $T^s_{Nl\pi}$ and $T^s_{Nl\delta}$ superseries in the H$^+$+ H system, and the values of $\Delta_{0,\text{tot}}$.

T^s_{Nlm}		$Nl \to N+2, l+2$	$N+2, l+2 \to N+4, l+4$	$N+4, l+4 \to N+6, l+6$	$\Delta_{0,\text{tot}}$
$T^s_{2p\pi}$	R_c	13.443;8.537	36.185;14.34	73.00;16.00	
	Δ_0	0.398	0.205	0.140	0.743
$T^s_{3p\pi}$	R_c	18.59;11.76	49.00;16.00		
	Δ_0	0.178	0.141		0.319
$T^s_{3d\pi}$	R_c	15.01;16.243	39.414;26.945	73.00;16.00	
	Δ_0	1.044	0.551	0.140	1.735
$T^s_{4d\pi}$	R_c	20.319;22.928	49;32		
	Δ_0	0.489	0.283		0.772
$T^s_{3d\delta}$	R_c	25.65;13.25	61.00;16.00		
	Δ_0	0.193	0.141		0.334
$T^s_{4f\delta}$	R_c	28.28;25.24	61.00;32.00		
	Δ_0	0.523	0.283		0.906

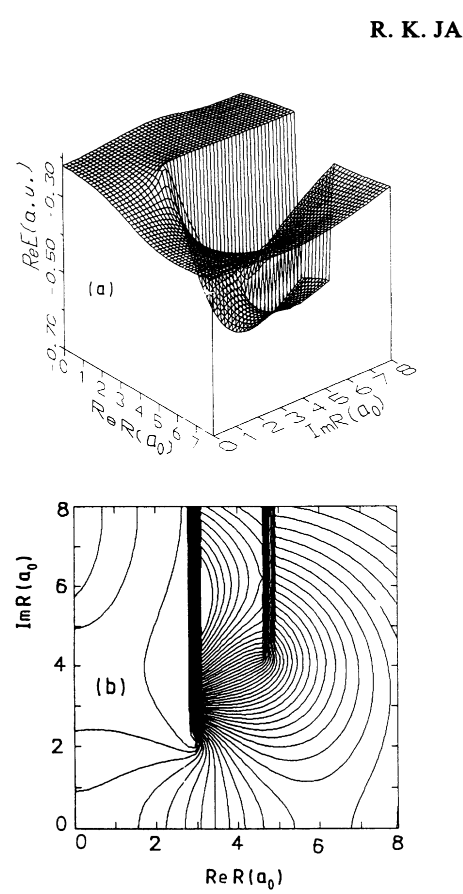

FIG. 9. (a) Three-dimensional and (b) contour plots of the $\mathrm{Re}E_{3d\sigma}(R)$ energy surface in the complex R plane, showing the $T(1s\sigma\text{-}3d\sigma)$ and $S(3d\sigma\text{-}4d\sigma)$ branching points (a) and corresponding branching cuts (b).

surface in the region $\mathrm{Re}R\sim5$, $\mathrm{Im}R\sim4$ is due to the T branching point (4.784; 4.143) connecting the $3d\sigma$ state with the $1s\sigma$ state (see Table IV). The singular behavior of the gradient of $\mathrm{Re}E_{3d\sigma}$ in the region $\mathrm{Re}R\sim3$, $\mathrm{Im}R\sim2$ is due to the S branching point (2.961; 1.965), connecting the states $3d\sigma$ and $4d\sigma$ (see Table I). The contour plot of $\mathrm{Re}E_{3d\sigma}(R)$, with $\Delta\,\mathrm{Re}E=0.01$, shown in Fig. 9(b), also shows the position of these branch points and the corresponding branch cuts.

III. TRANSITION PROBABILITIES AND COLLISION DYNAMICS

The transition probability between the adiabatic states $|\alpha\rangle$ and $|\beta\rangle$ connected by the complex branching point R_c is given in the adiabatic collision energy region by [2,4,9]

$$P_{\alpha\beta}=\exp(-2\Delta_{\beta\alpha}/v)\ , \tag{20}$$

where v ($\ll1$) is the relative collision velocity, and $\Delta_{\beta\alpha}$ is the generalized Massey parameter

$$\begin{aligned}\Delta_{\beta\alpha}&=\left|\mathrm{Im}\int_{\mathrm{Re}x(R_c)}^{x(R_c)}\Delta E_{\beta\alpha}(R(x))dx\right|\\&=\left|\mathrm{Im}\int_{C}E(R(x))dx\right|\ ,\end{aligned} \tag{21}$$

where $\Delta E_{\beta\alpha}(R)=E_\beta(R)-E_\alpha(R)$ is the difference of energies of adiabatic states, $x=vt=(R^2-b^2)^{1/2}$, with b being the impact parameter. The contour C in Eq. (21) starts at the real x axis [where $E(R)=E_\alpha(R)$], encompasses the branch point $x_c=x(R_c)$, and returns back to the real x axis, where $E(R)=E_\beta(R)$.

The quantity $\Delta_{\beta\alpha}$ is a function of impact parameter b, and for a given value of b it can be calculated (for $\mathrm{Re}R_c>0$) by using the available codes [6]. In the region $b\ll|R_c|$, the Massey parameter $\Delta_{\beta\alpha}(b)$ can be expanded as [11]

$$\Delta_{\beta\alpha}(b)\simeq\Delta_{\beta\alpha}(0)\left[1+\frac{b^2}{2|R_c|^2}\right]\ , \tag{22a}$$

where $\Delta_{\beta\alpha}(0)$ is given by Eq. (12), and for many S and T branch points in the H^++H system is tabulated in Tables I and II and Tables IV and V, respectively. We found that

$$\Delta_{\beta\alpha}(b)\simeq\frac{\Delta_{\beta\alpha}(0)}{\mathrm{Im}R_c}\,\mathrm{Im}(R_c^2-b^2)^{1/2} \tag{22b}$$

fits better the numerically calculated $\Delta_{\beta\alpha}(b)$ in a wide region of b values not necessarily much smaller than $|R_c|$. The square-root dependence in the last formula can be derived analytically from Eq. (21), if one assumes flatness and parallelness of neighboring complex energy branches (which is obviously true, except in the vicinity of R_c; see Figs. 3, 4, 5, and 7).

It has been shown [7] that $\Delta_{\beta\alpha}(0)$ for the S and T series can be approximated as

$$\Delta_{\beta\alpha}^{(S)}(0)\simeq|\Delta E_{\beta\alpha}(\,\mathrm{Re}R_c)\,\mathrm{Im}R_c|\ , \tag{23}$$

$$\Delta_{\beta\alpha}^{(T)}(0)\simeq|(\pi/4)\Delta E_{\beta\alpha}(\,\mathrm{Re}R_c)\,\mathrm{Im}R_c|\ . \tag{24}$$

We have also checked these formulas by comparing their results with those from the direct calculations of the individual $\Delta_{0,i}$ for many S and T series with $N\leq4$ and found that they are very accurate.

Equations (20), (23), and (24) show that for a branch point with a large imaginary part the transition probability is small. It should be kept in mind, however, that the factor $\Delta E_{\beta\alpha}(\,\mathrm{Re}R_c)$ in Eqs. (22), (23), and (24) may decrease with changing $\mathrm{Re}R_c$, so that the effect of increasing $\mathrm{Im}R_c$ on $p_{\alpha\beta}$ may not be so strong. This is the case with the $S_{lm}^{(\kappa)}$ series, for which both $\mathrm{Re}R_c^{(\kappa)}$ and $\mathrm{Im}R_c^{(\kappa)}$ change considerably, but $|R_c^{(\kappa)}|$ does not (see Fig. 2).

With the knowledge of the transition probability $p_{\alpha\beta}$ at each branching point, the simplest approach to the adiabatic collision dynamics is to follow the distribution of the incoming flux along different reaction paths. Since the position of "transition" points (the branching points in the complex R plane) is exactly known, and $p_{\alpha\beta}$ is calculated through the contour integral (21), the problem of overlapping transition regions, which appears in the usual multiple pseudocrossing treatments, does not exist. Even for the closely lying branch points of the S_{lm} series, the corresponding generalized Massey parameters can be calculated exactly. The evolution of the system outside the immediate vicinity of the branch points is strictly adiabatic. The question of accumulation of adiabatic phases in state population amplitudes is ruled out for the regions between the S branching points (since they are very close to each other), while the branch points of T superseries are always sufficiently far from each other (see Fig. 8) so that under slow collision conditions a phase averaging is allowed.

Although legitimate in the adiabatic limit ($v \rightarrow 0$) [4,10], this approach obviously oversimplifies the collision dynamics at finite collision velocities, and becomes invalid for $v \geq \Delta_{\beta\alpha}$. The coupled-channel formulation of the problem in the complex t plane would require tremendous computational efforts, as discussed in the introduction. It is, therefore, justifiable at this stage of the development of the concept of nonadiabatic transitions at the hidden crossings to adopt a simplified approach to the collision dynamics in order to explore the potential of the concept. (A more detailed discussion of the relation of this approach to the coupled-channel formalism based on dynamical molecular states can be found in Ref. [18].)

Apart from the transitions through the S and T branch points (which couple states with same values of the quantum number m), the rotational transitions in the region $R \rightarrow 0$ [between the states of a given (Nl) manifold with m quantum numbers differing by one] should also be included in the collision dynamics.

In the present work we have calculated the rotational probabilities within a given (Nl) manifold by solving numerically the coupled equations for the transition amplitudes $A_{\beta}^{\mathrm{rot}}(t)$, resulting from the expansion of time-dependent electron wave function over the united-atom basis functions [19]. The rotational coupling matrix elements in this basis have simple forms [19], while the state energies, to the first order in R, are given by [4]

$$E_{Nlm} = -\frac{(Z_1+Z_2)^2}{2N^2} - \gamma R^2 , \tag{25}$$

$$\gamma = \frac{2Z_1Z_2(Z_1+Z_2)^2[l(l+1)-3m^2]}{N^3 l(l+1)(2l-1)(2l+1)(2l+3)} . \tag{26}$$

We have solved the corresponding system of coupled equations for $A_{\beta}^{\mathrm{rot}}(t)$ (see Ref. [19]) by using Eq. (25) to represent the molecular energy, and the probability for the rotational transition $(Nlm_{\alpha}) \rightarrow (Nlm_{\beta})$ has been determined as

$$p_{\alpha\beta}^{\mathrm{rot}} = |A_{\beta}^{\mathrm{rot}}(t \rightarrow +\infty)|^2 . \tag{27}$$

IV. EXCITATION OF $n \leq 4$ STATES IN $H^+ + H$ COLLISIONS

A. General considerations

In the present section we shall apply the asymptotic approach discussed in the preceding section to calculate the cross sections for excitation of the $n=2,3,4$ levels of a hydrogen atom in slow collisions with protons, as well as for the proton-impact-induced transitions between these excited states. The number of S and T branching points connecting the H_2^+ molecular states which in the separated-atom limit go over to the $n=2,3,4$ manifolds is over 100, and about 85 of them have been considered important in the present calculations.

In the calculations of channel probabilities shown below, the transitions at the S and T branching points have been treated on equal footing. This means that following an $S_{lm}^{(\kappa)}$ sequence of branch points, the probability flux entering in that sequence does not necessarily end in the continuum in its entirety. Rather, at each subsequent $R_{Nlm}^{(\kappa)}$ branch point the flux is divided into $p_{Nlm}^{(S,\kappa)}$ and $(1-p_{Nlm}^{(S,\kappa)})$ parts which further evolve independently. If we are interested, however, only in the probability for ionization $p_{N_c lm}^{i(S,\kappa)}$ along the series $S_{N_c lm}^{(\kappa)}$, starting from the state $|N_c lm\rangle$, $N_c \geq l+1$ (or, equivalently, for the probability $1-p_{N_c lm}^{i(S,\kappa)}$), the multiplication of the transition probabilities of the form (19) gives

$$\begin{aligned} p_{N_c lm}^{i(S,\kappa)} &= \prod_{j=N_c}^{\infty} \exp(-2\Delta_{jlm}^{(\kappa)}/v) \\ &= \exp(-2\Delta_{N_c lm}^{\mathrm{tot},(\kappa)}/v) , \end{aligned} \tag{28}$$

where

$$\Delta_{N_c lm}^{\mathrm{tot},(\kappa)} = \sum_{j=N_c}^{\infty} \Delta_{jlm}^{(\kappa)} . \tag{29}$$

Having in mind the definition (21) of $\Delta_{jlm}^{(\kappa)}$ and the fact that $R_{jlm}^{(\kappa)} \simeq R_{\infty lm}^{(\kappa)}$ for all $j \geq N_c$, one obtains [10]

$$\Delta_{N_c lm}^{\mathrm{tot},(S,\kappa)} \simeq |E_{N_c lm}(\mathrm{Re} R_{\infty lm}^{(\kappa)}) \,\mathrm{Im}[(R_{\infty lm}^{(\kappa)})^2 - b^2]^{1/2}| . \tag{30a}$$

Expressions analogous to (28) and (29) apply also to the ionization probability $p_{N_c lm}^{i(T)}$ due to the superpromotion along a T superseries. In that case instead of Eq. (30a), we have used the expression

$$\Delta_{N_c lm}^{\mathrm{tot},(T)} \simeq \Delta_{N_c lm}(b) + \sum_{i=1}^{\infty} [\Delta_{N_c+i,lm}(0) - \Delta_{N_c lm}(0)] , \tag{30b}$$

where for $\Delta_{N_c lm}(b)$ the expression (22b) is used.

B. Excitation transitions from the ground state

Within the concept of collision dynamics described in Sec. III, we have considered the following proton-impact-induced excitation transitions from the ground-state hydrogen atom:

$$H^+ + H(1s) \rightarrow H^+ + H(2s, \text{ or } 2p) \tag{31}$$

$$\rightarrow H^+ + H(3s, p, \text{ or } 3d) \tag{32}$$

$$\rightarrow H^+ + H\ (n=4) . \tag{33}$$

In Fig. 10 we show part of the potential-energy diagram for the molecular states involved in the above transitions (only for the states going to the $n=2$ and $n=3$ separated-atom manifolds), as well as the most important S and T branch-point couplings. The initial-state probability flux splits equally between the $1s\sigma_g$ and $2p\sigma_u$

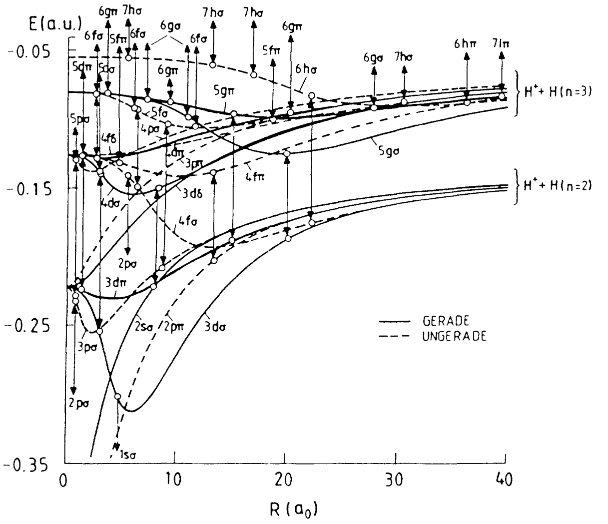

FIG. 10. Partial potential-energy diagram of H_2^+ system, emphasizing the potential curves correlated to the $n=2$ and $n=3$ manifolds and showing the transitions due the hidden crossings.

states during the incoming part of the trajectory, and for $R \leq 6$ part of it is transferred to the upper-lying states through the $T_{2p\sigma,4f\sigma}$, $T_{1s\sigma,3d\sigma}$, and $S_{2p\sigma,3p\sigma}$ branch points and through the $2p\sigma_u$-$2p\pi_u$ rotational coupling. The probability flux transferred to the upper states evolves further according to the distribution of the branching points connecting the higher states. During the receding stage of the collision, the probability fluxes (population probabilities) propagating along various molecular states are further redistributed when the system passes through the coupling regions. The probability P_{Nlm} for population of a given asymptotic state $|Nlm\rangle$ consists, therefore, of many reaction paths. In what follows, the elementary transition probability at a given branching point $R_{Nlm}^{N'l'm}$ will be denoted as $p_{Nlm,N'l'm}$. The character of the branching point (S or T type) can be distinguished on the basis of selection rules ($N'=N+1$, $l'=l$ for an S branch point, and $N'=N+2$, $l'=l+2$ for a T branch point). In the case of S branch points, the superscript κ will appear in $p_{Nlm,N+1lm}$ only when $\kappa \geq 1$. The probability for a rotational transition $|Nlm\rangle \rightarrow |Nlm'\rangle$ $(m'=m\pm 1)$ will carry a superscript "rot," while the probability for promotion to the continuum starting with the $|N_c lm\rangle$ state will be denoted as in Eq. (28).

1. *Excitation of 2s and 2p states*

From the six molecular states shown in Fig. 10 which asymptotically go into the $n=2$ separated-atom states, only four ($2s\sigma_g$, $2p\pi_u$, $3p\sigma_u$, and $3d\sigma_g$) effectively lead to population of the $n=2$ level in reaction (31). The $4f\sigma_u$ state is coupled with the $2p\sigma_u$ state at $\mathrm{Re}R \simeq 5.44$ by a very weak T coupling (see Table IV), and when populated it is quickly promoted to the continuum or decays within the $N=4$ manifold of states. The rotational coupling $3d\pi_g$-$3d\sigma_g$ is also very weak with respect to the other couplings populating the above-mentioned four molecular states. Neglecting also some other weak couplings, the asymptotic population probabilities of the $2s\sigma$, $2p\pi$, $3p\pi$, and $3d\sigma$ states can be written as (see Fig. 10)

$$P_{2s\sigma} \simeq \tfrac{1}{2} p_{1s\sigma,3d\sigma} p_{3d\sigma,4d\sigma} (1-p_{3d\sigma,4d\sigma})(1-p_{4d\sigma,5d\sigma})^2 p_{4d\sigma,2s\sigma} + \tfrac{1}{2} p_{1s\sigma,3d\sigma} p_{3d\sigma,4d\sigma} p_{4d\sigma,2s\sigma} , \tag{34}$$

$$P_{2p\pi} \simeq \tfrac{1}{2}(1-p_{2p\sigma,3p\sigma}) p_{2p\sigma,2p\pi}^{\mathrm{rot}} (1-p_{2p\pi,4f\pi})(1-p_{2p\sigma,4f\sigma}) , \tag{35}$$

$$\begin{aligned} P_{3p\sigma} \simeq {} & \tfrac{1}{2} p_{2p\sigma,3p\sigma} (1-p_{2p\sigma,3p\sigma})(1-p_{3p\sigma,4p\sigma})^2 (1-p_{3p\sigma,5f\sigma})(1-p_{2p\sigma,4f\sigma}) \\ & + \tfrac{1}{2} p_{2p\sigma,3p\sigma} p_{3p\sigma,4p\sigma} (1-P_{4p\sigma}^{i}) p_{3p\sigma,4p\sigma} (1-p_{2p\sigma,4f\sigma})(1-p_{3p\sigma,5f\sigma}) , \end{aligned} \tag{36}$$

$$\begin{aligned} P_{3d\sigma} \simeq {} & \tfrac{1}{2} p_{1s\sigma,3d\sigma} (1-p_{1s\sigma,3d\sigma})(1-p_{3d\sigma,5g\sigma}) + \tfrac{1}{2} p_{1s\sigma,3d\sigma} (1-p_{3d\sigma,4d\sigma})^2 (1-p_{1s\sigma,3d\sigma})(1-p_{3d\sigma,5g\sigma}) \\ & + \tfrac{1}{2} p_{1s\sigma,3d\sigma} p_{3d\sigma,4d\sigma} (1-P_{4d\sigma}^{i}) p_{3d\sigma,4d\sigma} (1-p_{1s\sigma,3d\sigma})(1-p_{3d\sigma,5g\sigma}) , \end{aligned} \tag{37}$$

where the factor $\frac{1}{2}$ appears due to equal population of the initial $1s\sigma_g$ and $2p\sigma_u$ states. We note that at asymptotically large R the above molecular states are linear combination (with equal weight) of two atomic states centered on the target and the projectile. Therefore, only one-half of the probabilities (34)–(37) are associated with the excitation channels.

The excitation probabilities P_{2s} and P_{2p} are obtained by first connecting the $|Nlm\rangle$ states with the $|nn_1n_2m\rangle$ parabolic states and then projecting the corresponding population probabilities to the separated-atom angular momentum states $|nl_a m\rangle$. Using the numerical values of the corresponding Clebsch-Gordan coefficients [9] and having in mind the above remark, one obtains

$$P_{2s} = \tfrac{1}{4}(P_{2s\sigma} + P_{3p\sigma} + P_{3d\sigma}) , \tag{38}$$

$$P_{2p} = \tfrac{3}{2}[0.408^2(P_{2s\sigma} + P_{3p\sigma} + P_{3d\sigma}) + 0.577\,35^2 P_{2p\pi}] . \tag{39}$$

When integrating these probabilities over the impact parameter b to obtain the cross sections σ_{2s} and σ_{2p}, the exact values of $\Delta_{Nlm,N'l'm}(b)$ in the region $b \leq R_{Nlm}^{N'l'm}$ were used in the expressions for $P_{Nlm,N'lm}$. [$\Delta_{Nlm,N'l'm}(b)$ were calculated for a large number of b, allowing a highly accurate fit to an appropriate analytic expression.]

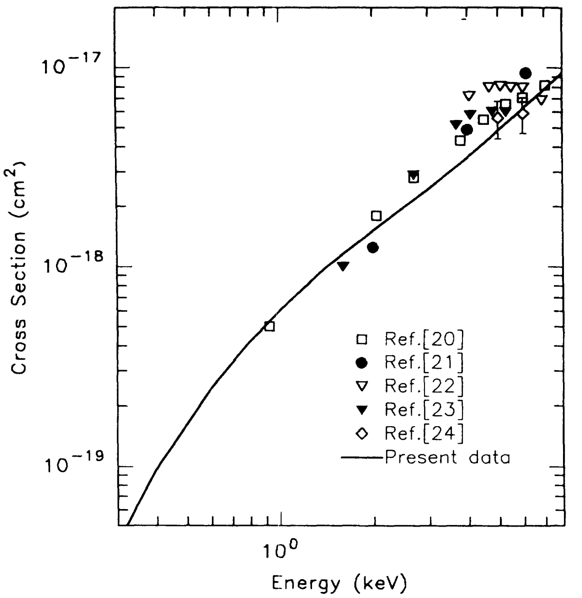

FIG. 11. Cross section for $1s \rightarrow 2s$ excitation in $H^+ + H(1s)$ collisions. The solid line represents the present results; open diamonds are experimental data of Morgan, Geddes, and Gilbody [24]. Other symbols are theoretical data from Refs. [20] (□), [21] (●), [22] (▽), and [23] (▼).

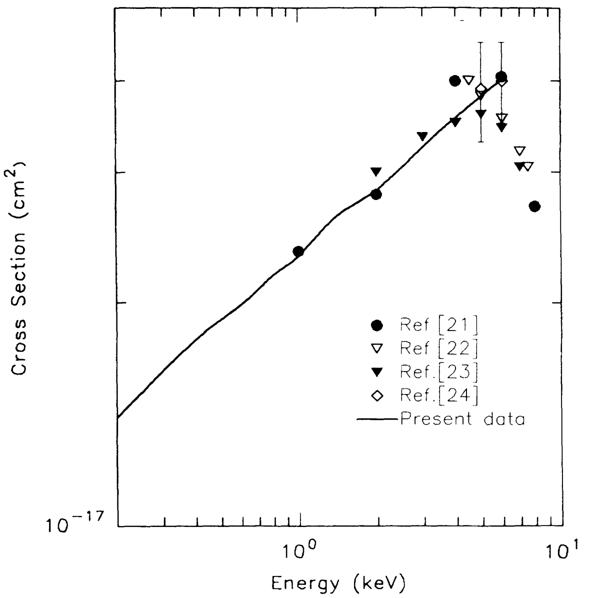

FIG. 12. Cross section for excitation of the $n=2$ hydrogen level in $H^+ + H(1s)$ collisions. The solid line represents the present results; open diamonds are experimental data of Morgan, Geddes, and Gilbody [24]. Other symbols are theoretical data from Refs. [21] (●), [22] (▽), and [23] (▼).

The cross section for excitation of the 2*s* state is shown in Fig. 11 (the solid line), and is compared with the results of other calculations [20–23] and with the experimental data of Morgan, Geddes, and Gilbody [24]. The present results in the region 1–8 keV agree within 10% with the results of the 10-molecular-orbital (MO) coupled-channel calculations of Kimura and Thorson [20].

The main contribution to σ_{2s} comes from the $3d\sigma$ reaction channel which is dominantly populated by the $T_{1s\sigma,3d\sigma}$ transition at Re$R \simeq 4.8$. The $3p\sigma$ channel also gives an appreciable contribution to σ_{2s}, since the promotion to continuum along the $S_{2p\sigma}$ series is not too strong.

In the case of the 2*p* excitation, the main contribution to the cross section in the region below 8 keV gives the $2p\pi$ channel populated by the strong $2p\sigma$-$2p\pi$ rotational coupling at small Re*R*. At energies above 8 keV, the probability flux along the $2p\pi$ reaction channel is significantly reduced due to the promotion of that molecular state along the $T^s_{2p\pi}$ superseries. For $E \geq 15$ keV, the main contribution to σ_{2p} gives the $3d\sigma$ and $3p\sigma$ channels.

In Fig. 12 we give the total excitation cross section $\sigma_2 = \sigma_{2s} + \sigma_{2p}$ for the energy range 0.2–5 keV, where the contribution of σ_{2s} is about 10% or less. The comparison of present results with those from the multistate atomic orbital coupled-channel calculations, using both two-center [21,22] and three-center [23] expansion, shows a good agreement in the region 1–5 keV.

2. *Excitation of the n = 3 and n = 4 levels*

The reaction channels $5g\sigma$ and $4f\pi$, populated via the $T_{1s\sigma,3d\sigma} \times T_{3d\sigma,5g\sigma}$ and $(2p\sigma$-$2p\pi) \times T_{2p\pi,4f\pi}$ transitions, respectively, give the dominant contribution to the excitation of the $n=3$ hydrogen level at low energies. Neglecting certain weak couplings, the probabilities of these reaction channels are (cf. Fig. 10)

$$P_{5g\sigma} \simeq \tfrac{1}{2}[p_{1s\sigma,3d\sigma}(1-p_{3d\sigma,4d\sigma})^2(1-p^{\mathrm{rot}}_{3d\sigma,3d\pi})(1-p_{1s\sigma,3d\sigma})p_{3d\sigma,5g\sigma} + (1-p_{1s\sigma,3d\sigma})p_{1s\sigma,3d\sigma}p_{3d\sigma,5g\sigma}](1-p_{5g\sigma,7i\sigma}) , \tag{40}$$

$$P_{4f\sigma} \simeq \tfrac{1}{2}(1-p_{2p\sigma,3p\sigma})p^{\mathrm{rot}}_{2p\sigma,2p\pi}p_{2p\pi,4f\pi}(1-p_{4f\pi,6h\pi})(1-p_{2p\sigma,4f\sigma}) . \tag{41}$$

The corresponding excitation probabilities of the atomic angular-momentum states 3*s*, 3*p*, and 3*d* can be expressed in terms of $P_{5g\sigma}$ and $P_{4f\sigma}$ as

$$P_{3s} = \tfrac{1}{6}P_{5g\sigma} , \tag{42a}$$

$$P_{3p} = \tfrac{1}{4}(P_{4f\pi} + P_{5g\sigma}) , \tag{42b}$$

$$P_{3d} = \tfrac{1}{4}(P_{4f\pi} + \tfrac{1}{3}P_{5g\sigma}) . \tag{42c}$$

The values of the cross sections σ_{3s}, σ_{3p}, σ_{3d}, and their

TABLE VI. Values of the σ_{3l} and σ_3 excitation cross sections of ground-state hydrogen by proton impact. The numbers in brackets denote multiplicative powers of ten.

E (keV)	σ_{3s} (cm^2)	σ_{3p} (cm^2)	σ_{3d} (cm^2)	σ_3 (cm^2)
0.2	2.20[−22]	1.82[−21]	1.60[−21]	3.65[−21]
0.4	3.31[−21]	2.13[−20]	1.80[−20]	4.26[−20]
0.6	1.05[−20]	6.40[−20]	5.36[−20]	1.28[−19]
0.8	2.02[−20]	1.25[−19]	1.04[−19]	2.49[−19]
1	3.13[−20]	1.95[−19]	1.64[−19]	3.90[−19]
1.4	5.39[−20]	3.57[−19]	3.05[−19]	7.16[−19]
2	8.57[−20]	5.95[−19]	5.16[−19]	1.20[−18]
3	1.33[−19]	9.90[−19]	8.91[−19]	2.01[−18]
4	1.83[−19]	1.35[−18]	1.25[−18]	2.78[−18]
6	3.08[−19]	1.95[−18]	1.87[−18]	4.13[−18]
8	4.73[−19]	2.58]−18]	2.50[−18]	5.55[−18]
10	6.68[−19]	3.18[−18]	3.06[−18]	6.90[−18]
14	1.10[−18]	4.34[−18]	4.08[−18]	9.51[−18]
20	1.75[−18]	5.88[−18]	5.31[−18]	1.29[−17]

sum σ_3 are given in Table VI for the energy range from 0.2 to 20 keV. Below 10 keV, the σ_{3s} cross section gives a small contribution (10% or less) to the total cross section, reflecting the fact that the $T_{1s\sigma,3d\sigma}$ transition in this energy region is much weaker than the rotational $2p\sigma$-$2p\pi$ coupling. The total $n=3$ excitation cross section is shown in Fig. 13. In the region above 12 keV, the cross section σ_3 can be compared with the extensive [40 atomic orbitals (AO)] two-center-expansion coupled-channel calculations of Fritsch and Lin [22], and the agreement is good. In the energy range 15–25 keV, the present results also agree with the experimental data of Park *et al.* [25], normalized according to Shakeshaft [26] (the normalization factor being 0.91). The coupled-channel calculations of Shakeshaft [26], using scaled hydrogenic functions, are also shown in the figure.

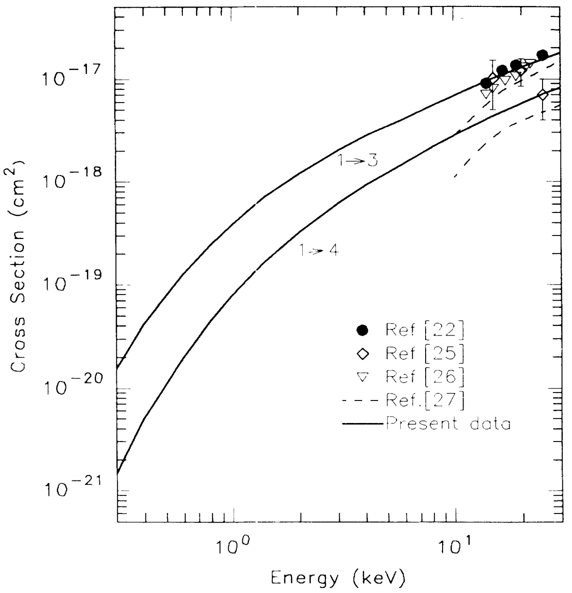

FIG. 13. Excitation of the $n=3$ and $n=4$ hydrogen levels in $H^+ + H(1s)$ collisions. Solid lines are the present results and open diamonds are experimental data of Park *et al.* [25] normalized as in Ref. [26]. Other symbols are theoretical data from Refs. [22] (●), [26] (▽), and [27] (dashed lines).

The main contribution to the excitation of the $n=4$ level in $H^+ + H(1s)$ collisions gives the reaction channels $6h\pi$ (originating from the $2p\sigma$-$2p\pi$ coupling) and $7i\sigma$ (originating from the $T_{1s\sigma,3d\sigma}$ transition). The $7i\sigma$ and $6h\pi$ channel probabilities are constructed similarly to those for the $5g\sigma$ and $4f\sigma$, channels, respectively. $P_{7i\sigma}$ can be obtained by replacing the factor $(1-p_{5g\sigma,7i\sigma})$ in Eq. (40) by $p_{5g\sigma,7i\sigma}(1-p_{7i\sigma,9k\sigma})$, and $P_{6h\pi}$ is obtained from Eq. (41) by replacing the last two factors $(1-p_{4f\pi,6h\pi})(1-p_{2p\sigma,4f\sigma})$ by $p_{4f\pi,6h\pi}(1-p_{6h\pi,8j\pi})$. The calculated excitation cross section $\sigma_4=\sigma_{6h\pi}+\sigma_{7i\sigma}$ is shown in Fig. 13 (solid line) and its value at $E=25$ keV agrees with the experimental result of Park *et al.* [25]. The σ_4 cross section is compared with the recent calculations of Reinhold *et al.* [27] (dashed line) performed by using the symmetrized eikonal approximation. This approximation is not expected to be valid below 20 keV/amu since it accounts for only the direct transitions.

C. Cross sections for $n=2 \rightarrow n'=3,4$ and $n=3 \rightarrow n'=4$ transitions

The analysis of the strength of various couplings connecting the molecular states correlated with the $n=2$ manifold of atomic states showed that in the population of the reaction channels leading to excitation of the $n=3$ level only the following initial molecular states have to be considered: $2s\sigma$, $2p\pi$, $3p\sigma$, $3d\sigma$, and $3d\pi$. The significantly populated molecular states correlating to the $n=3$ level are $4d\sigma$, $5f\sigma$, $5g\sigma$, $3p\pi$, $4f\pi$, and $5g\pi$. The main couplings connecting the above initial and final states are $T_{2s\sigma,4d\sigma}$, $T_{3p\sigma,5f\sigma}$, $T_{3d\sigma,5g\sigma}$, $T_{2p\pi,4f\pi}$, $T_{3d\pi,5g\pi}$, and the $3p\sigma$-$3p\pi$ rotational coupling. [In the redistribution of the initial probability flux (weighted by $\frac{1}{8}$ for the σ states and by $\frac{1}{4}$ for the π states) along various reaction paths, many other transitions have also to be included.] The total excitation probability for the 2→3 transition can be written as

$$P(2\rightarrow 3)=\tfrac{1}{2}[P_\sigma(2\rightarrow 3)+P_\pi(2\rightarrow 3)] , \tag{43}$$

$$P_\sigma(2\rightarrow 3)=P_{4d\sigma}+P_{5f\sigma}+P_{5g\sigma} , \tag{44a}$$

$$P_\pi(2\rightarrow 3)=P_{3p\pi}+P_{4f\pi}+P_{5g\pi} , \tag{44b}$$

where the probabilities $P_{Nl\sigma}$ and $P_{Nl\pi}$ are given in Appendix A.

The excitation of the $n=4$ level from $n=2$ has dynamics similar to the excitation of the $n=3$ level, except that the promotion of the system along the T superseries is now extended with one additional T-type transition. The dominant reaction channels populating the $n=4$ level are $6g\sigma$ (dominated by the $T_{2s\sigma,4d\sigma}\times T_{4d\sigma,6g\sigma}$ transitions), $7h\sigma$ (dominated by $T_{3p\sigma,5f\sigma}\times T_{5f\sigma,7h\sigma}$), $7i\sigma$ (through $T_{3d\sigma,5g\sigma}\times T_{5g\sigma,7i\sigma}$), $6h\pi$ (through $T_{2p\pi,4f\pi}\times T_{4f\pi,6h\pi}$), $7i\pi$ (through $T_{3d\pi,5g\pi}\times T_{5g\pi,7i\pi}$), and $5f\pi$ (through $3p\sigma$-$3p\pi$ rotational coupling, followed by the $T_{3p\pi,5f\pi}$ transition).

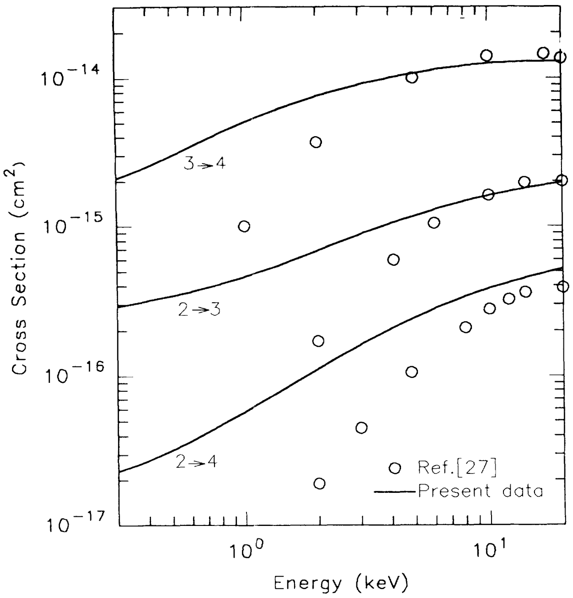

FIG. 14. Cross sections for $n \rightarrow n'$ transitions in $H^+ + H\ (n)$ collisions. Solid curves are the present results; open circles are the data from Ref. [27].

The 2→4 transition probability is, therefore,

$$P(2\rightarrow4)=\tfrac{1}{2}[P_\sigma(2\rightarrow4)+P_\pi(2\rightarrow4)] \tag{45}$$

with

$$P_\sigma(2\rightarrow4)=P_{6g\sigma}+P_{7h\sigma}+P_{7i\sigma}\ , \tag{46a}$$

$$P_\pi(2\rightarrow4)=P_{5f\pi}+P_{6h\pi}+P_{7i\pi}\ , \tag{46b}$$

where $P_{Nl\sigma}$ and $P_{Nl\pi}$ are given in Appendix A.

The cross sections of the 2→3 and 2→4 transitions in the energy range 0.2–20 keV are shown in Fig. 14 (solid lines). At energies above 10 keV, the calculated cross sections are close to those of the symmetrized eikonal approximation [27]. As noted earlier, the eikonal approximation ceases to be valid for energies well below the energy at which the cross-section maximum appears ($\sim$20–25 keV for these transitions).

The excitation of $n=4$ level from $n=3$ includes coupling of a plethora of initial and final molecular states. The most important states involved in the population of the $n=4$ level are shown in Table VII. The number of S and T branching points which need to be included in the description of the process is over 100. The higher-order $S_{lm}^{(\kappa)}$ ($\kappa=1,2$) series (notably $S_{fm}^{(\kappa)}$, $S_{gm}^{(\kappa)}$, $S_{hm}^{(\kappa)}$) are also involved in the collision dynamics of the process, as are several $Nlm \rightarrow Nlm'(m,m'=0,1,2,\ \Delta m=\pm1)$ rotational couplings. The expression for the 3→4 transition probability is too complex to be displayed here. The total cross section for 3→4 excitation in the energy range 0.2–20 keV is shown in Fig. 14 and compared with the results of symmetrized eikonal approximation [27] available down to 1 keV.

TABLE VII. Initial and final molecular states considered in the $H(n=3)\rightarrow H(n=4)$ excitation by proton impact.

Initial states	Final states
$4p\sigma,4d\sigma,5f\sigma,5g\sigma,6h\sigma$	$5p\sigma,5d\sigma,6f\sigma,6g\sigma,7h\sigma,7i\sigma,8j\sigma$
$3p\pi,4d\pi,4f\pi,5g\pi$	$5f\pi,6g\pi,6h\pi,7i\pi$
$3d\delta,4f\delta$	$5f\delta,5g\delta,6h\delta$

V. IONIZATION OF H(1s) AND H* ($n=2,3$) BY PROTONS

In the present section we shall apply the "hidden-crossings" adiabatic method to calculate the cross sections of the following ionization processes:

$$H^+ + H(1s)\rightarrow H^+ + H^+ + e\ , \tag{47}$$

$$H^+ + H^*(2s,\ \text{or}\ 2p)\rightarrow H^+ + H^+ + e\ , \tag{48}$$

$$H^+ + H^*(3s,\ 3p,\ \text{or}\ 3d)\rightarrow H^+ + H^+ + e\ . \tag{49}$$

In the energy range 5–25 keV, reaction (47) has been studied previously by Ovchinnikov [11] by using the same method. Here, we extend the calculations down to 0.2 keV to compare the results of this method with the recent extensive (150-MO's) coupled-channel calculations of Kimura and Thorson [28].

In reaction (47) the system initially evolves along the $1s\sigma$ molecular state and at $\mathrm{Re}R \simeq 4.8$ it undergoes the $T_{1s\sigma,3d\sigma}$ transition (see Table IV). At $\mathrm{Re}R \simeq 3$ the system starts the promotion along the $S_{3d\sigma}$ series and reaches the continuum at $\mathrm{Re}R \simeq 2.7$. The part of initial flux in the molecular state $1s\sigma$ that has avoided the $T_{1s\sigma,3d\sigma}$ transition is subject to superpromotion to the continuum along the $T_{1s\sigma}^{s}$ (or $T_{00}^{(g)}$) superseries during the receding of the nuclei. The system $H^+ + H(1s)$ evolving along the initial molecular state $2p\sigma$ meets first the transition point $T_{2p\sigma,4f\sigma}$ at $\mathrm{Re}R \simeq 5.44$ (see Table IV). Because of the large value of the corresponding Massey parameter ($\Delta_0 \simeq 3.5$, see Table IV), the transition probability $p_{2p\sigma,4f\sigma}$ is negligibly small in the entire adiabatic energy region. At $\mathrm{Re}R \simeq 0.8$ the system enters the superpromotion region of the $S_{p\sigma}$ superseries. The unpromoted part of the flux is subject to the $2p\sigma$-$2p\pi$ rotational transition and the outgoing flux on the $2p\pi$ molecular state can be promoted to the continuum via the $T_{2p\pi}^{s}$ superseries.

The probability of the ionization process (47) can, therefore, be written as

$$P_{\text{ion}}(1s)=P_{1s\sigma}^{\text{ion}}+P_{2p\sigma}^{\text{ion}} \tag{50}$$

with

$$\begin{aligned}P_{1s\sigma}^{\text{ion}} = \tfrac{1}{2}[&p_{1s\sigma,3d\sigma}P_{d\sigma}^{i(S)}+(1-p_{1s\sigma,3d\sigma})P_{1s\sigma}^{i(T)}+p_{1s\sigma,3d\sigma}(1-p_{3d\sigma,4d\sigma})^2(1-p_{3d\sigma,3d\pi}^{\text{rot}})(1-p_{1s\sigma,3d\sigma})P_{3d\sigma}^{i(T)}\\ &+p_{1s\sigma,3d\sigma}(1-p_{3d\sigma,4d\sigma})(p_{3d\sigma,3d\pi}^{\text{rot}}P_{3d\pi}^{i(T)}+p_{3d\sigma,3d\pi}^{\text{rot}}p_{3d\pi,3d\delta}^{\text{rot}}P_{3d\delta}^{i(T)})]\ ,\end{aligned} \tag{51}$$

$$P_{2p\sigma}^{\text{ion}} \simeq \tfrac{1}{2}[P_{p\sigma}^{i(S)}+(1-p_{2p\sigma,3p\sigma})p_{2p\sigma,2p\pi}^{\text{rot}}P_{2p\pi}^{i(T)}+p_{2p\sigma,3p\sigma}(1-p_{3p\sigma,4p\sigma})^2(1-p_{2p\sigma,3p\sigma})P_{3p\sigma}^{i(T)}]\ , \tag{52}$$

where $P^{i(S)}_{lm}$ and $P^{i(T)}_{Nlm}$ are the probabilities for superpromotion to the continuum along the corresponding S and T superseries.

The calculated ionization cross section $\sigma_{\text{ion}}(1s)$ is shown in Fig. 15 (solid line). It is compared with the results of the 40-AO-based two-center [22] and triple-center [23] coupled-channel calculations, with the results of the 150-MO coupled-channel calculations by Kimura and Thorson [28] and with the experimental data by Shah *et al.* [29]. The agreement of the present results with the experimental data in the overlapping energy region is found to be very good, as well as with the results of 150-MO-based coupled-channel calculations [28] in the region below 3 keV.

The cross sections for proton-impact ionization of H*(2s) and H*(2p) excited atoms have been calculated in a similar manner. Referring to Fig. 10, and keeping in mind that the statistical weights of σ and π molecular states correlating with the $n=2$ separated-atom states are $\frac{1}{8}$ and $\frac{1}{4}$, respectively, the probabilities for ionization of 2s and 2p states are

$$P_{\text{ion}}(2s)=\tfrac{1}{16}(P^{\text{ion}}_{2s\sigma}+P^{\text{ion}}_{3p\sigma}+P^{\text{ion}}_{3d\sigma}+P^{\text{ion}}_{4f\sigma})\ , \qquad (53)$$

$$P_{\text{ion}}(2p)=\tfrac{1}{4}(P^{\text{ion}}_{2p\pi}+P^{\text{ion}}_{3d\pi}) + \tfrac{1}{16}(P^{\text{ion}}_{3d\sigma}+P^{\text{ion}}_{4f\sigma}+P^{\text{ion}}_{2s\sigma}+P^{\text{ion}}_{3p\sigma})\ , \qquad (54)$$

where P^{ion}_{Nlm} are the ionization probabilities for particular initial molecular states, given in Appendix B.

TABLE VIII. Ionization cross sections for H*(2s), H*(2p), and H* ($n=2$) in collisions with protons. The numbers in brackets denote multiplicative powers of ten.

E (keV)	$\sigma_{\text{ion}}(2s)$ (cm^2)	$\sigma_{\text{ion}}(2p)$ (cm^2)	$\sigma_{\text{ion}}(n=2)$ (cm^2)
0.2	1.795[−18]	1.953[−18]	3.748[−18]
0.4	6.484[−18]	8.131[−18]	1.461[−17]
0.6	1.282[−17]	1.781[−17]	3.063[−17]
0.8	2.011[−17]	3.024[−17]	5.035[−17]
1.0	2.801[−17]	4.490[−17]	7.291[−17]
1.4	4.509]−17]	7.977[−17]	1.249[−16]
2.0	7.282[−17]	1.434[−16]	2.162[−16]
3.0	1.227[−16]	2.690[−16]	3.917[−16]
4.0	1.749[−16]	4.077[−16]	5.826[−16]
6.0	2.792[−16]	6.949[−16]	9.740[−16]
8.0	3.781[−16]	9.723[−16]	1.350[−15]
10.0	4.699[−16]	1.231[−15]	1.701[−15]
14.0	6.327[−16]	1.689[−15]	2.321[−15]
20.0	8.339[−16]	2.253[−15]	3.087[−15]

The cross sections for ionization of H*(2s) and H*(2p) excited atoms by proton impact in the energy range 0.2–20 keV are given in Table VIII together with their sum. The dominant ionization channels in the entire energy range considered are the $4f\sigma$ and $3d\sigma$ channels, associated with the powerful superpromotion series $S^{(\kappa)}_{4f\sigma}$, $S^{(\kappa)}_{5g\sigma}$, and $S^{(\kappa)}_{6h\sigma}$. The total ionization cross section for the $n=2$ level is shown in Fig. 16 (solid line), together with the results of classical-trajectory Monte Carlo (CTMC) calculations [30] (open circles). Having in mind that the CTMC results are, generally speaking, reliable to within 30% in the region of the cross-section maximum and less reliable for energies below the maximum (the CTMC cross section decreases too rapidly), one may expect that the present results below ~6 keV are accurate (at least) to within 30%.

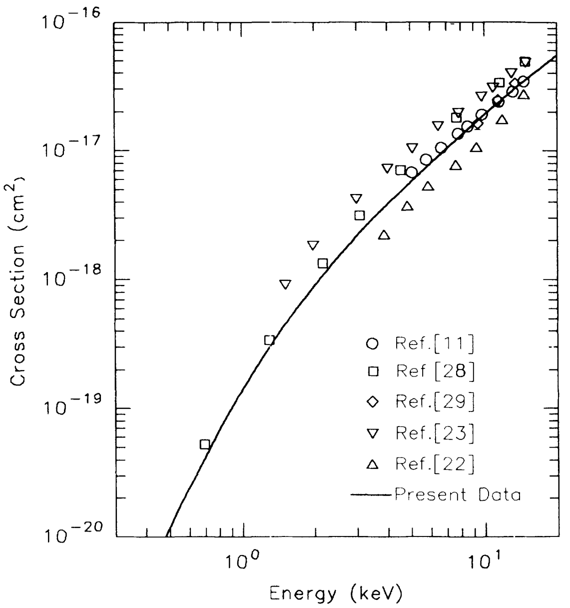

FIG. 15. Cross section for ionization of H(1s) by proton impact. The solid curve represents the present results; open diamonds are experimental data of Shah *et al.* [29]. Other symbols are theoretical data from Refs. [11] (○), [22] (△), [23] (▽), and [28] (□).

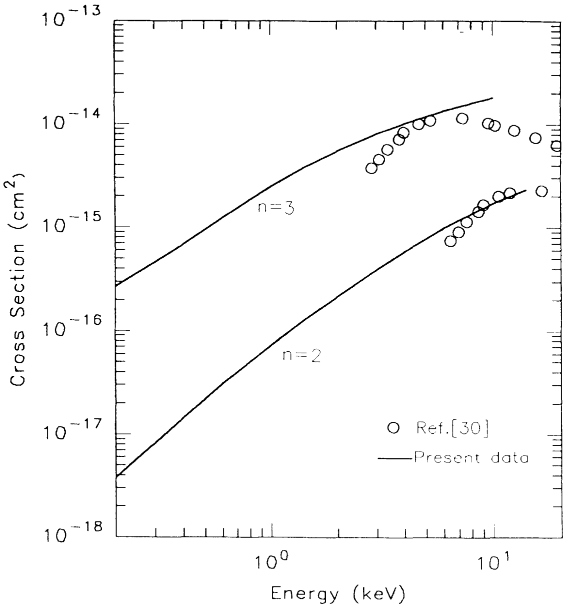

FIG. 16. Cross sections for ionization of H ($n=2$) and H ($n=3$) by proton impact. Solid lines: present results; open circles: results of classical-trajectory Monte Carlo (CTMC) calculations [30].

The ionization of the $n=3$ level of a hydrogen atom by proton impact proceeds through a large number of superpromotion channels. From all molecular states which correlate with the $n=3$ separated-atom manyfold of states, only $3p\pi$ and $3d\delta$ do not have a promoting character. Among the most promotive S series which originate from states correlating with $n=3$ are $S^{(\kappa)}_{5f\sigma}$, $S^{(\kappa)}_{5g\sigma}$, $S^{(\kappa)}_{6h\sigma}$, $S^{(0)}_{4f\pi}$, and $S^{(\kappa)}_{5f\pi}$. T-type transitions to molecular states correlated with the $n=2$ and $n=4,5$ separated-atom manifolds of states introduce additional superpromoting S series into the $n=3$ ionization process (e.g., $S_{3d\sigma}$ through the $T_{5g\sigma,3d\sigma}$ transition, $S^{(\kappa)}_{7h\sigma}$ through the $T_{5f\sigma,7h\sigma}$ transition, etc.). During the receding of nuclei, superpromotion of the system to continuum takes place along several strong T^s superseries (such as $T^s_{3p\pi}$, $T^s_{4d\pi}$, $T^s_{4p\sigma}$, $T^s_{4f\pi}$, etc.). The expression for the ionization probability of the $n=3$ level can be written as

$$P_{\text{ion}}(n=3)=P_{\text{ion}}(3s)+P_{\text{ion}}(3p)+P_{\text{ion}}(3d)\ , \tag{55}$$

$$P_{\text{ion}}(3s)=\tfrac{1}{54}(P^{\text{ion}}_{3s\sigma}+P^{\text{ion}}_{4p\sigma}+P^{\text{ion}}_{4d\sigma}+P^{\text{ion}}_{5f\sigma}+P^{\text{ion}}_{5g\sigma}+P^{\text{ion}}_{6h\sigma})\ , \tag{56}$$

$$P_{\text{ion}}(3p)=\tfrac{1}{36}(P^{\text{ion}}_{3s\sigma}+P^{\text{ion}}_{4p\sigma}+P^{\text{ion}}_{5g\sigma}+P^{\text{ion}}_{6h\sigma}+P^{\text{ion}}_{7i\sigma})+\tfrac{1}{18}(P^{\text{ion}}_{3p\pi}+P^{\text{ion}}_{4d\pi}+P^{\text{ion}}_{4f\pi}+P^{\text{ion}}_{5g\pi})\ , \tag{57}$$

$$\begin{aligned}P_{\text{ion}}(3d)=&\tfrac{1}{96}(P^{\text{ion}}_{3s\sigma}+P^{\text{ion}}_{4p\sigma}+P^{\text{ion}}_{5g\sigma}+P^{\text{ion}}_{6h\sigma}+P^{\text{ion}}_{7i\sigma})+\tfrac{1}{27}(P^{\text{ion}}_{4d\sigma}+P^{\text{ion}}_{5f\sigma})\\&+\tfrac{1}{18}(P^{\text{ion}}_{3p\pi}+P^{\text{ion}}_{4d\pi}+P^{\text{ion}}_{4f\pi}+P^{\text{ion}}_{5g\pi})+\tfrac{1}{9}(P^{\text{ion}}_{3d\delta}+P^{\text{ion}}_{4f\delta})\ ,\end{aligned} \tag{58}$$

where the initial molecular state ionization probabilities P^{ion}_{Nlm} have a very complex structure to be presented here, and the numerical coefficients in front of the parentheses in Eqs. (56)–(58) include both the statistical weights and the corresponding Clebsch-Gordan coefficients. The values of the ionization cross sections $\sigma_{\text{ion}}(3s)$, $\sigma_{\text{ion}}(3p)$, and $\sigma_{\text{ion}}(3d)$ in the energy range 0.2–20 keV are given in Table IX. The total cross section for ionization of the $n=3$ level is shown in Fig. 16. The results of present calculations agree well with the CTMC results [30] (also shown in Fig. 16) in the energy region around the cross-section maximum and should be accurate to within (30–40)% for lower energies.

VI. CONCLUDING REMARKS

In the present paper we have investigated the dynamics of excitation and ionization processes in slow $H^{+}+H$ (n), $n\leq 3$, collisions by using the asymptotic method and the concept of hidden crossings of adiabatic potential-energy surfaces in the complex plane of internuclear distance. We have studied in detail the topology of the S and T series of hidden crossings in the (H^{+},e,H^{+}) system in the entire complex R plane. All hidden crossings, or series of such crossings, contributing significantly to the inelastic processes studied have been taken into account in the cross-section calculations. The rotational transitions in the united-atom region have been treated within the close-coupling formalism.

TABLE IX. Ionization cross sections for $H^{*}(3s$, $3p$, or $3d)$ and $H^{*}(n=3)$ in collisions with protons. The numbers in brackets denote multiplicative powers of ten.

E (keV)	$\sigma_{\text{ion}}(3s)$ (cm^2)	$\sigma_{\text{ion}}(3p)$ (cm^2)	$\sigma_{\text{ion}}(3d)$ (cm^2)	$\sigma_{\text{ion}}(n=3)$ (cm^2)
0.2	6.805[−17]	1.164[−16]	8.388[−17]	2.683[−16]
0.4	1.474[−16]	2.814[−16]	2.573[−16]	6.861[−16]
0.6	2.342[−16]	4.854[−16]	5.047[−16]	1.224[−15]
0.8	3.238[−16]	7.121[−16]	7.963[−16]	1.832[−15]
1.0	4.134[−16]	9.481[−16]	1.108[−15]	2.469[−15]
1.4	5.866[−16]	1.420[−15]	1.739[−15]	3.745[−15]
2.0	8.237[−16]	2.082[−15]	2.629[−15]	5.535[−15]
3.0	1.159[−15]	3.031[−15]	3.901[−15]	8.091[−15]
4.0	1.435[−15]	3.816[−15]	4.947[−15]	1.020[−14]
6.0	1.866[−15]	5.047[−15]	6.584[−15]	1.350[−14]
8.0	2.195[−15]	5.987[−15]	7.828[−15]	1.601[−14]
10.0	2.459[−15]	6.738[−15]	8.821[−15]	1.802[−14]
14.0	2.863[−15]	7.883[−15]	1.032[−14]	2.107[−14]
20.0	3.283[−15]	9.067[−15]	1.185[−14]	2.420[−14]

The comparison of the obtained results for the processes considered with the available experimental data and with the results of extensive coupled-channel calculations shows that the present method adequately describes the collision dynamics of the $H^{+}+H$ (n) collision system in the adiabatic energy region. The agreement of the present results is always better with those from the large-base coupled-channel calculations which incorporate molecular effects (such as the MO and triple-center expansion methods) than with the results of two-center AO-expansion calculations. The observed good agreement of the present results with the experimental data and with the MO calculations indicates that the basic assumption of the method (i.e., localized transitions at the complex branching points and adiabatic evolution outside their immediate vicinity) seems to be acceptable.

The range of applicability of the present method as described in Sec. III is limited on the low-energy side by the validity of the adopted semiclassical approximation. On the high-energy side, the applicability of the method is limited by the assumption about the adiabatic development of the system. In practice, this assumption is justified for $v\leq\Delta_{0,m}$ where $\Delta_{0,m}$ is the minimum value of all $\Delta_{0,i}$ which appear in the expression for a given channel probability. This criterion simply requires that all transition probabilities involved in the dynamics are exponentially small.

ACKNOWLEDGMENTS

We would like to thank Dr. E. A. Solov'ev for providing us with his computer code TERM. Many useful discussions with Dr. T. P. Grozdanov are also gratefully acknowledged.

APPENDIX A: CHANNEL EXCITATION PROBABILITIES IN $n=2\rightarrow n'=3,4$ TRANSITIONS

The molecular-channel excitation probabilities entering Eqs. (44) for the $n=2\rightarrow n'=3$ transition are given by

$$P_{4d\sigma}=\tfrac{1}{8}[(1-p_{2s\sigma,4d\sigma})p_{2s\sigma,4d\sigma}(1-p_{4d\sigma,6g\sigma})+p_{2s\sigma,4d\sigma}(1-p_{3d\sigma,4d\sigma})^2(1-p_{4d\sigma,5d\sigma})^2(1-p_{2s\sigma,4d\sigma})(1-p_{4d\sigma,6g\sigma})]\ , \tag{A1}$$

$$\begin{aligned}P_{5f\sigma}=\tfrac{1}{8}[&(1-p_{3p\sigma,5f\sigma})(1-p_{2p\sigma,3p\sigma})^2(1-p_{3p\sigma,4p\sigma})^2(1-p^{\text{rot}}_{3p\sigma,3p\pi})p_{3p\sigma,5f\sigma}(1-p_{5f\sigma,7h\sigma})\\&+p_{3p\sigma,5f\sigma}(1-p^{(1)}_{5f\sigma,4f\sigma})^2(1-p^{(1)}_{5f\sigma,6f\sigma})^2(1-p_{4f\sigma,5f\sigma})^2(1-p_{5f\sigma,6f\sigma})^2\\&\times(1-p_{3p\sigma,5f\sigma})(1-p_{5f\sigma,7h\sigma})(1-p^{\text{rot}}_{5f\sigma,5f\pi})]\ ,\end{aligned} \tag{A2}$$

$$\begin{aligned}P_{5g\sigma}=\tfrac{1}{8}[&(1-p_{3d\sigma,5g\sigma})(1-p_{1s\sigma,3d\sigma})^2(1-p_{3d\sigma,4d\sigma})^2(1-p^{\text{rot}}_{3d\sigma,3d\pi})p_{3d\sigma,5g\sigma}(1-p_{5g\sigma,7i\sigma})\\&+p_{3d\sigma,5g\sigma}(1-p^{(0)}_{5g\sigma,6g\sigma})(1-p^{(1)}_{5g\sigma,6g\sigma})^2(1-p_{3d\sigma,5g\sigma})(1-p_{5g\sigma,7i\sigma})]\ ,\end{aligned} \tag{A3}$$

$$P_{3p\pi}=\tfrac{1}{8}(1-p_{3p\sigma,5f\sigma})(1-p_{2p\sigma,3p\sigma})(1-p_{3p\sigma,4p\sigma})p^{\text{rot}}_{3p\sigma,3p\pi}(1-p_{3p\pi,5f\pi})\ , \tag{A4}$$

$$P_{4f\pi}=\tfrac{1}{4}[(1-p_{2p\pi,4f\pi})(1-p^{\text{rot}}_{2p\sigma,2p\pi})p_{2p\pi,4f\pi}(1-p_{4f\pi,6h\pi})p_{2p\pi,4f\pi}(1-p_{4f\pi,5f\pi})^2(1-p_{4f\pi,6h\pi})(1-p^{\text{rot}}_{4f\sigma,4f\pi})]\ , \tag{A5}$$

$$\begin{aligned}P_{5g\pi}=\tfrac{1}{4}[&(1-p_{3d\pi,5g\pi})(1-p_{3d\pi,4d\pi})^2(1-p^{\text{rot}}_{3d\sigma,3d\pi})p_{3d\pi,5g\pi}(1-p_{5g\pi,7i\pi})\\&+p_{3d\pi,5g\pi}(1-p_{4g\pi,5g\pi})^2(1-p^{(1)}_{4g\pi,5g\pi})^2(1-p_{3d\pi,5g\pi})(1-p_{5g\pi,7i\pi})(1-p^{\text{rot}}_{5g\pi,5g\delta})]\ .\end{aligned} \tag{A6}$$

The molecular-channel excitation probabilities entering Eqs. (46) for the $n=2\rightarrow n'=4$ transition are given by

$$P_{6g\sigma}=\tfrac{1}{8}[(1-p_{2s\sigma,4d\sigma})p_{2s\sigma,4d\sigma}P_{4d\sigma,6g\sigma}+p_{2s\sigma,4d\sigma}(1-p_{3d\sigma,4d\sigma})^2(1-p_{4d\sigma,5d\sigma})^2(1-p_{2s\sigma,4d\sigma})p_{4d\sigma,6g\sigma}(1-p_{6g\sigma,8i\sigma})]\ , \tag{A7}$$

$$\begin{aligned}P_{7h\sigma}=\tfrac{1}{8}[&(1-p_{3p\sigma,5f\sigma})(1-p_{2p\sigma,3p\sigma})^2(1-p_{3p\sigma,4p\sigma})^2(1-p^{\text{rot}}_{3p\sigma,3p\pi})p_{3p\sigma,5f\sigma}P_{5f\sigma,7h\sigma}(1-p_{7h\sigma,9j\sigma})\\&+p_{3p\sigma,5f\sigma}(1-p^{(0)}_{5f\sigma,6f\sigma})^2(1-p^{(1)}_{5f\sigma,6f\sigma})^2(1-p^{(0)}_{4f\sigma,5f\sigma})^2(1-p^{(1)}_{4f\sigma,5f\sigma})^2(1-p_{3p\sigma,5f\sigma})\\&\times p_{5f\sigma,7h\sigma}(1-p^{\text{rot}}_{5f\sigma,5f\pi})(1-p_{7h\sigma,9j\sigma})]\ ,\end{aligned} \tag{A8}$$

$$\begin{aligned}P_{7i\sigma}=\tfrac{1}{8}[&(1-p_{3d\sigma,5g\sigma})(1-p_{1s\sigma,3d\sigma})^2(1-p_{3d\sigma,4d\sigma})^2(1-p^{\text{rot}}_{3d\sigma,3d\pi})p_{3d\sigma,5g\sigma}P_{5g\sigma,7i\sigma}(1-p_{7i\sigma,9k\sigma})\\&+p_{3d\sigma,5g\sigma}(1-p^{(0)}_{5g\sigma,6g\sigma})^2(1-p^{(1)}_{5g\sigma,6g\sigma})^2(1-p_{3d\sigma,5g\sigma})p_{5g\sigma,7i\sigma}(1-p_{7i\sigma,9k\sigma})]\ ,\end{aligned} \tag{A9}$$

$$P_{5f\pi}=\tfrac{1}{8}(1-p_{3p\sigma,5f\sigma})(1-p_{2p\sigma,3p\sigma})(1-p_{3p\sigma,4p\sigma})p^{\text{rot}}_{3p\sigma,3p\pi}P_{3p\pi,5f\pi}(1-p_{5f\pi,7h\pi})\ , \tag{A10}$$

$$P_{6h\pi}=\tfrac{1}{4}[(1-p_{2p\pi,4f\pi})(1-p^{\text{rot}}_{2p\pi,2p\sigma})p_{2p\pi,4f\pi}+p_{2p\pi,4f\pi}(1-p_{4f\pi,5f\pi})^2(1-p_{5f\pi,7h\pi})p_{4f\pi,6h\pi}(1-p^{\text{rot}}_{4f\sigma,4f\pi})](1-p_{6h\pi,8j\pi})\ , \tag{A11}$$

$$\begin{aligned}P_{7i\pi}=\tfrac{1}{4}[&(1-p_{3d\pi,5g\pi})(1-p_{3d\pi,4d\pi})^2(1-p^{\text{rot}}_{3d\sigma,3d\pi})p_{3d\pi,5g\pi}P_{5g\pi,7i\pi}\\&+p_{3d\pi,5g\pi}(1-p^{(0)}_{5g\pi,6g\pi})^2(1-p^{(1)}_{5g\pi,6g\pi})^2(1-p_{3d\pi,5g\pi})(1-p^{\text{rot}}_{5g\sigma,5g\pi})p_{5g\pi,7i\pi}](1-p_{7i\pi,9k\pi})\ .\end{aligned} \tag{A12}$$

APPENDIX B: INITIAL MOLECULAR-CHANNEL IONIZATION PROBABILITIES FOR THE $H^++H(n=2)\rightarrow H^++H^++e$ REACTION

$$P^{\text{ion}}_{2s\sigma}=p_{2s\sigma,4d\sigma}(1-p_{3d\sigma,4d\sigma})P^{i(S)}_{4d\sigma}+(1-p_{2s\sigma,4d\sigma})P^{i(T)}_{2s\sigma}\ , \tag{B1}$$

$$\begin{aligned}P^{\text{ion}}_{3p\sigma}=&(1-p_{3p\sigma,5f\sigma})(1-p_{2p\sigma,3p\sigma})P^{i(S)}_{3p\sigma}+p_{3p\sigma,5f\sigma}\\&\times[(1-p^{(0)}_{4f\sigma,5f\sigma})P^{i(S,0)}_{5f\sigma}+(1-p^{(0)}_{4f\sigma,5f\sigma})(1-p^{(0)}_{5f\sigma,6f\sigma})(1-p^{(1)}_{4f\sigma,5f\sigma})P^{i(S,1)}_{5f\sigma}]\\&+(1-p_{3p\sigma,5f\sigma})\{(1-p_{2p\sigma,3p\sigma})^2(1-p_{3p\sigma,4p\sigma})^2(1-p^{\text{rot}}_{3p\sigma,3p\pi})P^{i(T)}_{3p\sigma}+(1-p_{2p\sigma,3p\sigma})(1-p_{3p\sigma,4p\sigma})p^{\text{rot}}_{3p\sigma,3p\pi}P^{i(T)}_{3p\pi}\\&\qquad+(1-p_{2p\sigma,3p\sigma})p_{3p\sigma,4p\sigma}[(1-p_{4s\sigma,5p\sigma})^2+(1-p^{\text{rot}}_{3p\sigma,3p\pi})](1-p_{3p\sigma,4p\sigma})P^{i(T)}_{4p\sigma}\}\ ,\end{aligned} \tag{B2}$$

$$P^{\text{ion}}_{2p\pi}=p_{2p\pi,4f\pi}P^{i(S)}_{4f\pi}+(1-p_{2p\pi,4f\pi})(1-p^{\text{rot}}_{2p\pi,2p\sigma})P^{i(T)}_{2p\pi}+p_{2p\pi,4f\pi}(1-p_{2p\pi,4f\pi})(1-p_{4f\pi,5f\pi})^2P^{i(T)}_{4f\pi}\ , \tag{B3}$$

$$\begin{aligned}P^{\text{ion}}_{3d\pi}=&\,p_{3d\pi,5g\pi}[P^{i(S,0)}_{5g\pi}+(1-p^{(0)}_{5g\pi,6g\pi})P^{i(S,1)}_{5g\pi}]+(1-p_{3d\pi,5g\pi})\\&\times[(1-p^{\text{rot}}_{3d\pi,3d\sigma}-p^{\text{rot}}_{3d\pi,3d\delta})P^{i(T)}_{3d\pi}+p^{\text{rot}}_{3d\pi,3d\sigma}P^{i(T)}_{3d\delta}+p^{\text{rot}}_{3d\pi,3d\delta}P^{i(T)}_{3d\delta}]\\&+p_{3d\pi,5g\pi}(1-p_{3d\pi,5g\pi})(1-p^{(0)}_{5g\pi,6g\pi})^2(1-p^{(1)}_{5g\pi,6g\pi})^2P^{i(T)}_{5g\pi}\ ,\end{aligned} \tag{B4}$$

$$\begin{aligned}P^{\text{ion}}_{3d\sigma}=&\,(1-p_{3d\sigma,5g\sigma})(1-p_{1s\sigma,3d\sigma})P^{i(S)}_{3d\sigma}+p_{3d\sigma,5g\sigma}[P^{i(S,0)}_{5g\sigma}+(1-p^{(0)}_{5g\sigma,6g\sigma})P^{i(S,1)}_{5g\sigma}]\\&+(1-p_{3d\sigma,5g\sigma})\{(1-p_{1s\sigma,3d\sigma})^2(1-p_{3d\sigma,4d\sigma})^2(1-p^{\text{rot}}_{3d\sigma,3d\pi})P^{i(T)}_{3d\sigma}\\&\qquad+(1-p_{1s\sigma,3d\sigma})(1-p_{3d\sigma,4d\sigma})(p^{\text{rot}}_{3d\sigma,3d\pi}P^{i(T)}_{3d\pi}+p^{\text{rot}}_{3d\sigma,3d\pi}p^{\text{rot}}_{3d\pi,3d\delta}P^{i(T)}_{3d\delta})\\&\qquad+(1-p_{1s\sigma,3d\sigma})p_{3d\sigma,4d\sigma}(1-p_{3d\sigma,4d\sigma})[1-p^{\text{rot}}_{3d\sigma,3d\pi}+(1-p_{4d\sigma,5d\sigma})^2](1-p_{2s\sigma,4d\sigma})P^{i(T)}_{4d\sigma}\}\\&+p_{3d\sigma,5g\sigma}(1-p^{(0)}_{5g\sigma,6g\sigma})^2(1-p^{(1)}_{5g\sigma,6g\sigma})^2(1-p_{3d\sigma,5g\sigma})P^{i(T)}_{5g\sigma}\ ,\end{aligned} \tag{B5}$$

$$\begin{aligned}P^{\text{ion}}_{4f\sigma}=&\,(1-p_{4f\sigma,6h\sigma})[P^{i(S,0)}_{4f\sigma}+(1-p^{(0)}_{4f\sigma,5f\sigma})P^{i(S,1)}_{4f\sigma}]\\&+p_{4f\sigma,6h\sigma}[P^{i(S,0)}_{6h\sigma}+(1-p^{(0)}_{6h\sigma,7h\sigma})P^{i(S,1)}_{6h\sigma}+(1-p^{(0)}_{6h\sigma,7h\sigma})(1-p^{(1)}_{6h\sigma,7h\sigma})P^{i(S,2)}_{6h\sigma}]\\&+(1-p_{4f\sigma,6h\sigma})(1-p_{2p\sigma,4f\sigma})^2(1-p^{(0)}_{4f\sigma,5f\sigma})^2(1-p^{(1)}_{4f\sigma,5f\sigma})^2P^{i(T)}_{4f\sigma}\\&+p_{4f\sigma,6h\sigma}(1-p^{(0)}_{6h\sigma,7h\sigma})^2(1-p^{(1)}_{6h\sigma,7h\sigma})^2(1-p^{(2)}_{6h\sigma,7h\sigma})^2(1-p_{4f\sigma,6h\sigma})P^{i(T)}_{6h\sigma}\\&+(1-p_{4f\sigma,6h\sigma})\{p^{(0)}_{4f\sigma,5f\sigma}[(1-p^{(0)}_{5f\sigma,6f\sigma})^2(1-p^{(1)}_{5f\sigma,6f\sigma})^2(1-p^{(1)}_{4f\sigma,5f\sigma})^2+(1-p_{4f\sigma,5f\sigma})](1-p^{(0)}_{4f\sigma,5f\sigma})\\&\qquad+p^{(1)}_{4f\sigma,5f\sigma}[(1-p^{(1)}_{5f\sigma,6f\sigma})^2(1-p^{(0)}_{4f\sigma,5f\sigma})(1-p^{(0)}_{5f\sigma,6f\sigma})+1](1-p^{(0)}_{4f\sigma,5f\sigma})\\&\qquad\times(1-p^{(0)}_{5f\sigma,6f\sigma})(1-p^{(1)}_{4f\sigma,5f\sigma})\}(1-p_{3p\sigma,5f\sigma})P^{i(T)}_{5f\sigma}\ .\end{aligned} \tag{B6}$$

[1] B. H. Bransden, *Atomic Collision Theory,* 2nd ed. (Benjamin, New York, 1982).

[2] E. E. Nikitin and S. Ya Umanskii, *Theory of Slow Atomic Collisions,* Springer Series in Chemical Physics Vol. 30 (Springer-Verlag, Berlin, 1984).

[3] J. B. Delos, Rev. Mod. Phys. **53**, 287 (1981).

[4] E. A. Solov'ev, Usp. Fiz. Nuak **157**, 437 (1989) [Sov. Phys. Usp. **32**, 228 (1989)].

[5] E. A. Solov'ev and S. I. Vinitsky, J. Phys. B **18**, L557 (1985).

[6] E. A. Solov'ev, Zh. Eksp. Teor. Fiz. **81**, 1681 (1981) [Sov. Phys. JETP **54**, 893 (1981)].

[7] S. Yu. Ovchinnikov and E. A. Solov'ev, Zh. Eksp. Teor. Fiz. **90**, 921 (1986) [Sov. Phys. JETP **63**, 538 (1986)].

[8] E. A. Solov'ev, Zh. Eksp. Teor. Fiz. **90**, 1165 (1986) [Sov. Phys. JETP **63**, 678 (1986)].

[9] L. D. Landau and E. M. Lifshitz, *Quantum Mechanics: Non-Relativistic Theory,* 3rd ed. (Pergamon, Oxford, 1965).

[10] T. P. Grozdanov and E. A. Solov'ev, Phys. Rev. A **42**, 2703 (1990).

[11] S. Yu. Ovchinnikov, Phys. Rev. A **42**, 3865 (1990).

[12] R. K. Janev and P. S. Krstic, Phys. Rev. A **44**, R1435 (1991).

[13] R. K. Janev, Comments At. Mol. Phys. **26**, 83 (1991).

[14] P. S. Krstic and R. K. Janev (unpublished).

[15] I. V. Komarov, L. I. Ponomarev, and S. Yu. Slavyanov, *Spheroidal and Coulomb Spheroidal Functions* (Nauka, Moscow, 1976) (in Russian).

[16] G. Henri, V. Sidis, and C. Kubach, J. Phys. B **18**, 691 (1985).

[17] U. Fano and W. Lichten, Phys. Rev. Lett. **14**, 627 (1965).

[18] T. P. Grozdanov and E. A. Solov'ev, Phys. Rev. A **44**, 5605 (1991).

[19] T. P. Grozdanov and E. A. Solov'ev, J. Phys. B **15**, 3871 (1982).

[20] M. Kimura and W. R. Thorson, Phys. Rev. A **24**, 1780 (1981).

[21] H. J. Lüdde and R. M. Dreizler, J. Phys. B **15**, 2703 (1982).

[22] W. Fritsch and C. D. Lin, Phys. Rev. A **27**, 3361 (1983).

[23] T. G. Winter and C. D. Lin, Phys. Rev. A **29**, 567 (1984).

[24] T. J. Morgan, J. Geddes, and H. B. Gilbody, J. Phys. B **6**, 2118 (1973).

[25] J. T. Park, J. E. Aldag, J. M. George, and J. L. Peacher, Phys. Rev. A **14**, 608 (1976).

[26] R. Shakeshaft, Phys. Rev. A **18**, 1930 (1978).

[27] C. O. Reinhold, R. E. Olson, and W. Fritsch, Phys. Rev. A **41**, 4837 (1990).

[28] The results of M. Kimura and W. R. Thorson quoted in M. Kimura and N. F. Lane, Adv. At. Mol. Phys. **26**, 79 (1990).

[29] M. B. Shah, D. S. Elliot, P. McCallion, and H. B. Gilbody, J. Phys. B **21**, 2455 (1988).

[30] R. E. Olson, J. Phys. B **13**, 483 (1980).